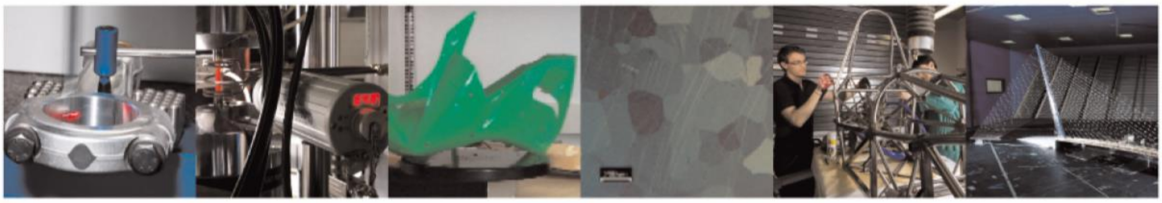

Effect of overhanging surfaces on the evolution of substrate topography and internal defects formation in laser powder bed fusion

Matteo Bugatti, Quirico Semeraro, Bianca Maria Colosimo

This is a post-peer-review, pre-copyedit version of an article published in Journal of Manufacturing Processes. The final authenticated version is available online at:
http://dx.doi.org/10.1016/j.jmapro.2022.03.030

Effect of overhanging surfaces on the evolution of substrate topography and internal defects formation in laser powder bed fusion

Matteo Bugatti[a,*], Quirico Semeraro[a], Bianca Maria Colosimo[a]

[a]*Dipartimento di Meccanica, Politecnico di Milano, via La Masa 1, 20156, Milano (MI), Italy*

Abstract

Overhanging (a.k.a. down-facing) surfaces are tipically found in complex metal parts built with laser powder bed fusion (L-PBF). When these surfaces exceed a certain extension or inclination with respect to the build plate, they need to be supported with external structures to avoid failure and macro-geometrical errors. However, a relatively large portion of the slice gets printed directly over loose powder, thus facing a substrate with significantly different wetting and heat transfer characteristics from solid/bulk. Several quality aspects (e.g., internal defects, surface topography) can be affected by the presence of overhangs, but their evolution during the process is still a relatively unexplored field. In this work, a new strategy based on process interruption is proposed for analyzing the evolution of defects produced during the printing of down-facing surfaces. Ex-situ high-accuracy characterization equipent was used to study their effect on the evolution of printed surface topography, internal defects, melted and sintered thickness. Results show that the process gradually recovers from the disturbance introduced by the overhang, but the peculiar structure of the internal defects observed in those regions reveals that even small unsupported areas can be detrimental to the as-built quality of the part. The combined use of surface topography data and volume reconstruction also allowed to develop and validate a physics-based model for predicting the evolution of surface topography and effective layer thickness in overhangs.

Keywords: Laser Powder Bed Fusion (L-PBF), Overhang, Roughness, Porosity

---

1. Introduction

Additive manufacturing (AM), and especially metal powder bed fusion, has revolutionized the manufacturing industry. Many industrial fields (e.g., aerospace, medical, oil and gas) can benefit from AM thanks to its unparalleled design freedom in fabricating complex and optimized metal parts that are lighter, stiffer, custom-made, and more cost-efficient than their predecessors.

Unfortunately, the manufacturing scheme for metal powder bed fusion presents some limitations when it comes to the fabrication of complex parts that include overhanging surfaces, i.e., portions of the layer that are printed directly on the powder bed without the support of solid material. The lack of solid material and the inherently lower heat conductivity of a metal powder substrate can introduce defects during the build, e.g heat accumulation, and collapse. If the portion of the layer printed directly on the powder bed exceeds a threshold value that depends on the geometry and the specific process parameters-machine-material combination, external structures are needed to support the overhanging surface.

---

[*] Corresponding author

Email addresses: `matteo.bugatti@polimi.it` (Matteo Bugatti), `quirico.semeraro@polimi.it` (Quirico Semeraro), `biancamaria.colosimo@polimi.it` (Bianca Maria Colosimo)

Nomenclature

ρ	Part density [%]
ρ_{pores}	Pores density, number of pores per unit volume [mm^{-3}]
ρ_{rel}	Relative density of powder w.r.t. solid metal [%]
A	Areal extension of the overhang [mm^2]
lt	Nominal layer thickness [µm]
lt_p	Nominal powder layer thickness [µm]
t_{mi}	i-th melted layer thickness of overhang sections [µm]
t_m	Equivalent melted layer thickness of overhang sections [µm]
t_{pi}	i-th powder layer thickness of overhang sections [µm]
t_s	Equivalent sintered thickness of overhang sections [µm]
V_m	Melted volume [mm^3]
V_s	Sintered volume [mm^3]
V_{pores}	Pores volume [mm^3]
Z_i	Depression depth in the overhang after layer i [µm]

External support structures can usually solve the problem but their design and their post-process removal must be carefully evaluated as they can add a significant cost to the build due to the increased waste material and post-processing required. In addition, when complex shapes are considered, adding external supports is not always a viable option where the surfaces they support are too fragile or when they are impossible to reach for removing the support (e.g., internal channels).

The most effective way to approach the problem is to redesign the feature itself to make it easier to manufacture. Since the early years of metal powder bed fusion, researchers have published survey papers and books on design for AM guidelines to collect all the process constraints and practical rules that should be followed to increase the geometrical and dimensional accuracy of an AM part and, in general, to improve its buildability. In the case of flat overhangs, redesigning usually involves the addition of chamfers or fillets to obtain a self-supporting part where the overhang does not exceed the maximum extensions suggested by the guidelines, i.e. 1-1,5 mm for overhangs supported only on one side [1, 2] and 3-5 mm for bridge-like dual-side supported overhangs [2, 3]. However, it should be pointed out that these threshold values have been mostly determined as the maximum overhang extension before build failure or formation of macro-geometrical defects on the external surface (e.g. excessive roughness, warping, sagging) and they do not consider other possible effects of the overhang on part quality.

Another approach proposed by researchers is to adapt the process parameters locally based on in-situ sensor readings (feedback control) or the output of analytical/numerical models (feed-forward control). In their seminal work, Kruth et al. [4] demonstrated that the implementation of a feedback control system in an L-PBF machine to monitor the size and the thermal emission of the melt pool makes it possible to adapt the laser beam power locally to print 5 mm long 0° overhangs without supports. A combination of in-situ monitoring and model-based control was used by Matthews et al. [5] to develop a feed-forward power control strategy for printing overhangs. DePond et al. [6] used the results of a thermomechanical simulation model by Hodge et al. [7] to reduce the power locally at a 6×6 mm^2 overhang. They demonstrated their approach effectively reduces sagging and dross formation in the final part. While feedback and feed-forward control of process parameters has been demonstrated to reduce the formation of surface defects, it is worth noting that these strategies are still limited to the lab environment and are not representative of the standard industrial settings this study will focus on. Still today, it is a common industrial practice to use fixed sets of process parameters for printing down-facing surfaces (or down skin), up-facing surfaces (or up skin), and bulk sections (Figure 1). Several studies on the optimization of those sets of parameters can be found in literature, with the majority of them running extensive experimental campaigns to explore the parameter space and using either external surface quality characteristics [8, 9, 10], dimensional accuracy [11] or part density [12] to evaluate their performance.

To the best of the authors' knowledge, the literature lacks studies investigating the evolution of defects induced by small overhangs using high-accuracy measuring equipment. Such a study would make it possible to investigate how the solidification progresses where the part is unsupported and to identify trends in the formation of defects, eventually providing valuable information for defect mitigation or part post-processing. So far, only a few works on AM in-situ monitoring have tackled the challenging task of studying the evolution of a defect during the process. DePond et al. [6] studied the evolution of surface topography when a relatively large flat overhang (6×6 mm^2) is manufactured, using an in-situ monitoring setup based on optical coherence tomography (OCT). Barrett et al. [15] mounted a surface profilometer on the recoater arm of an L-PBF machine to reconstruct the 3D map of the printed surface but, due to the high lateral resolution and vertical accuracy, the field of view (FOV) of this system was very limited ($<$ 20 mm). Other authors [16, 17] implemented a structured light setup in their experiments to reconstruct the surface quality but, in this case, the high resolution required limited the FOV. The evolution of internal defects was studied by Leung et al. [13] and Zhao et al. [14] using state-of-the-art equipment for in-situ high-speed synchrotron X-ray imaging, which allowed them to study the evolution of porosity at laser track level with an unprecedented level of resolution. Despite the novelty and the promising results of these recent works, their investigation relies on prototypal equipment and only focuses on one quality characteristic.

On the other hand, all the other works previously mentioned limit their assessment to the quality of the final part, without considering how the defects evolve during the process, thus leaving room for speculation on the underlying mechanisms of defect formation.

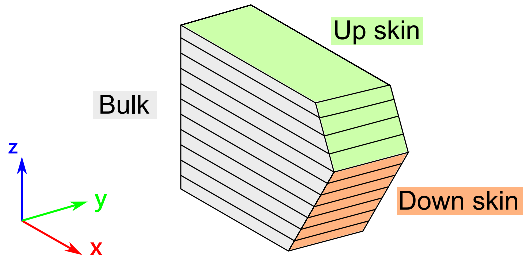

Figure 1: Down skin, up skin and bulk sections of a simple AM part built in vertical direction

In this study, a new strategy for analyzing the evolution of multiple defects when building complex features is proposed. Specifically, this work aims at:

1. Analyzing the influence of small ($\leq$ 15 mm^2) overhanging surfaces of different sizes built without supports on three potential classes of defects:
    - macro and micro-geometrical errors of the printed surface
    - internal defects formation (i.e. local pores)

   - partially-melted (sintered) powder

2. Quantitatively evaluating the evolution of the disturbance effect introduced by the overhangs in relation to the defects mentioned above as the process progresses

3. Providing insights about the underlying defect formation mechanisms via statistical analysis and physics-based modeling.

To perform these tasks, an experimental campaign was carried out using an industrial L-PBF machine with default process parameters to obtain results that are representative of true standard process conditions. The results of this work will make it possible to:

- improve the understanding of the effect of small overhangs on local product quality
- estimate the minimum overstock thickness required to avoid potentially defective regions in correspondence of the overhangs
- identify process signatures that may be leveraged for future in-situ defect detection.

In addition to these main results, to carry out some of the proposed analyses, a multi-modal segmentation-based method was developed for reconstructing and separating the volumes of multi-phase materials obtained via X-ray CT. This additional task was required to correctly reconstruct and distinguish between the fully-melted and partially-melted (sintered) regions that appear at the overhangs. Further details on the method developed are given in Section 3 and Appendix A.

The rest of the work is organized as follows:

- Section 2 explains the methodology implemented to approach the problem and how the experiment was designed and the equipment used to perform it and characterize the output of the experiment.
- Section 3 describes the procedures employed to characterize the specimens in terms of internal defects and surface quality. The results are analyzed and critically discussed in this section as well.
- Section 4 concludes the paper.

2. Experimental method, material and equipment

Studying the in-process evolution of an overhanging section in terms of substrate surface topography and internal defects would in principle require an in-situ monitoring setup. As discussed in the previous section, a few authors have started approaching the problem of in-situ substrate topography reconstruction using various techniques but, to date, the reconstruction of in-situ internal defects in part-scale specimens is not possible. To overcome this limitation and acquire both process signatures without the need for prototypal monitoring equipment, an experiment was designed to study the evolution of substrate topography and internal defects using off-line measuring instruments. The core idea of the experiment was to build a set of specimens with a variable number of layers after the beginning of the overhang (Figure 2a). In this way, each specimen is representative of a single phase in the layer-by-layer evolution of the overhang effect and can be analyzed in an off-line configuration. To achieve this goal and to study the effect of different sized overhangs, a bridge-like specimen was designed comprising unsupported sections of different lengths. The geometry of the specimen is shown in Figure 2.

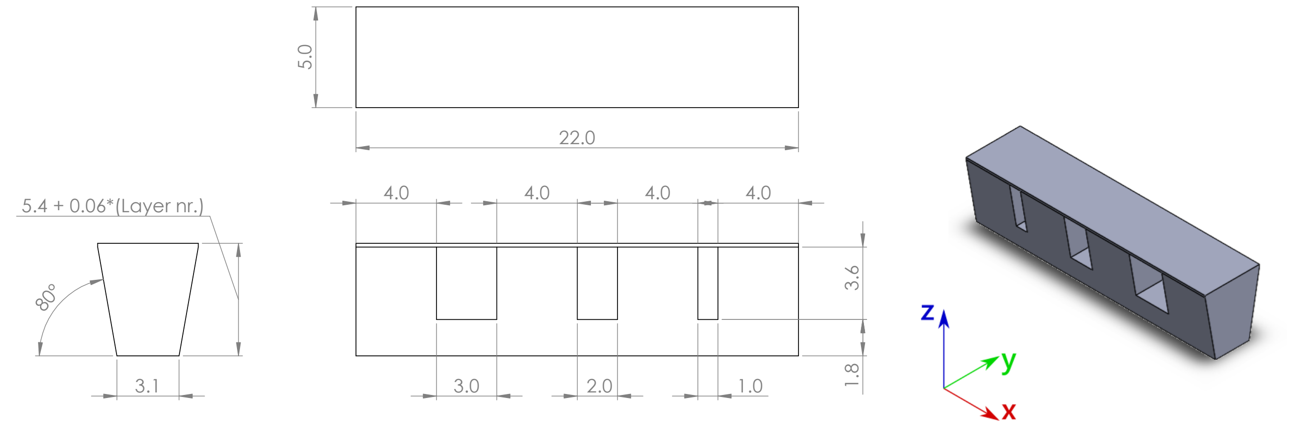

(a) Drawing (dimensions in mm). The final height of each specimen is variable and depends on the number of printed layers after the start of the overhang

(b) Isometric view

Figure 2: Specimen geometry

The experimental factors analyzed in this preliminary study and the corresponding level codes used for the following analyses are:

- *OH size*: overhang size, with 3 levels (1 mm, 2 mm and 3 mm) + the reference level 0, corresponding to the bulk (completely supported) condition
- *Layer no.*: number of layers after the start of the overhang, with 5 levels: 1, 2, 3, 4, 5

The experimental factors are also shown in Figure 3. It is worth to point out that, when choosing the levels for the *OH size* factor, the typical size limits suggested by the previously mentioned AM design guidelines for building completely unsupported overhanging surfaces were not exceeded.

2.1. Design of Experiment

Since the bridge-like specimen designed for the experiment already comprises all three levels of the *OH size* factor, the experimental design can focus only on the *Layer no.* factor and the 5 corresponding levels. To keep the variability that the position of the specimens could induce on the build plate under control, a Latin square design [18] was implemented to place replicas across the build plate evenly, i.e. one replica for each *Layer no.* level appears once in each X and Y position (see Figure 4). The resulting build plate consists of a 5×5 matrix of specimens where each level of the *Layer no.* factor was replicated 5 times. The additional 5-level blocking factors, X and Y that describe the specimen's position, can then be included in the analysis to keep their influence separated from that of the experimental factors. The coding of the two blocking factors is shown in Figure 4.

2.2. Materials and equipment

The specimens were manufactured using Ti6Al4V (15-45 µm) powder and a Renishaw AM250 industrial AM machine, equipped with a 200 W pulsed laser. Default process parameters were used for the experiment (Table 1), with locally optimized settings for printing down-skin sections of the layer, i.e. all overhangs. Up-skin parameters were disabled to avoid remelting the last layer of the specimen, which would compromise its representativeness

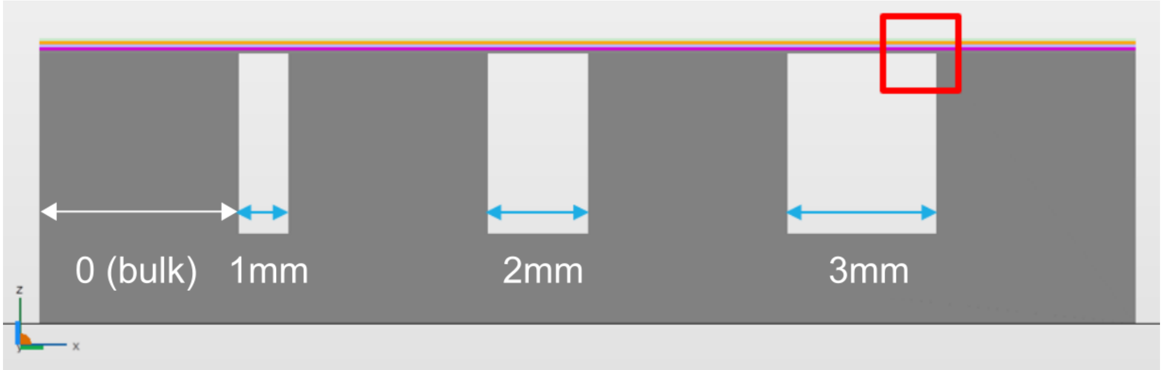

(a) OH size

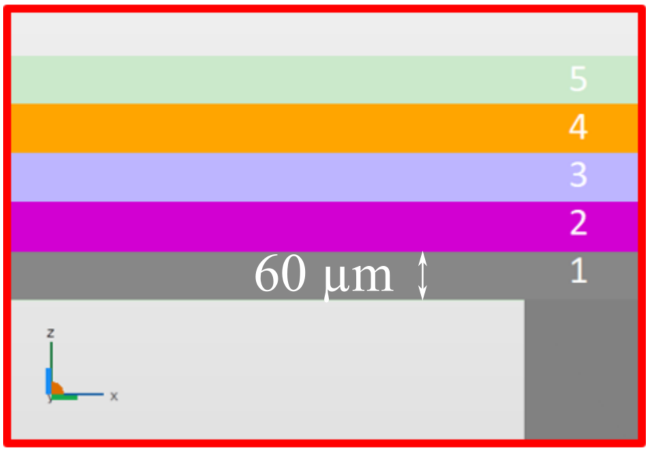

(b) Layer no.

Figure 3: Experimental factors

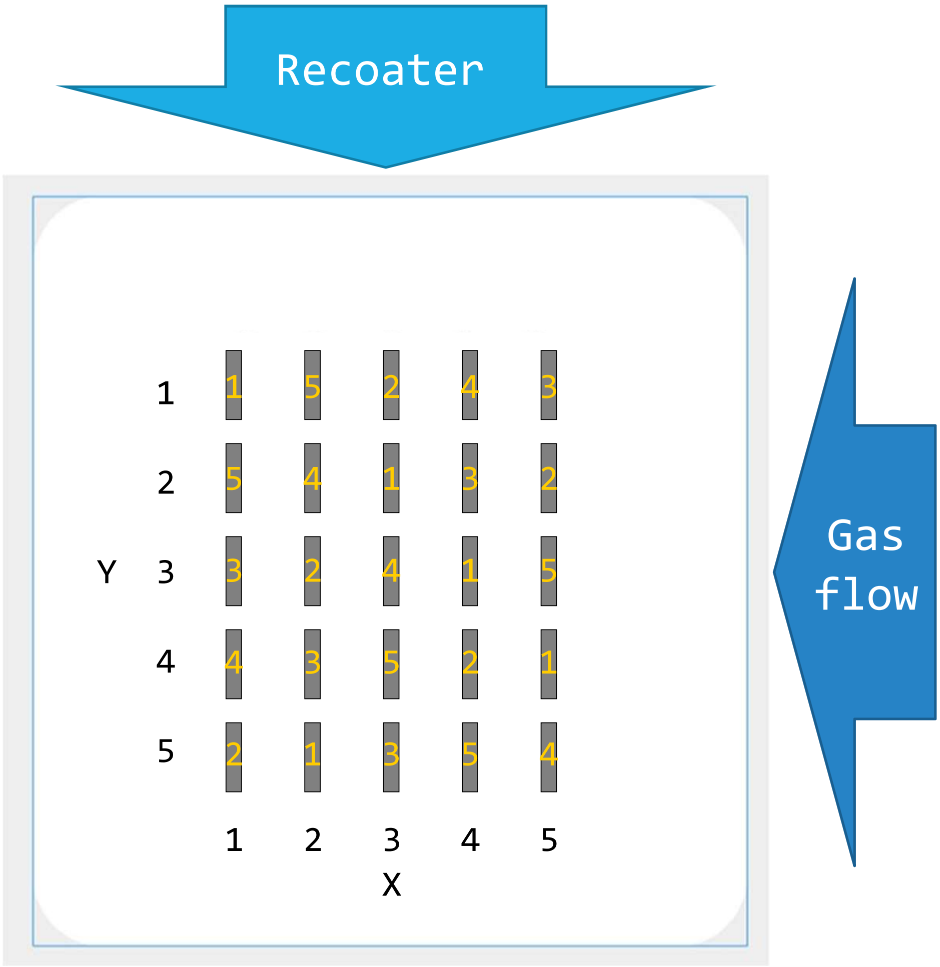

Y \ X	1	2	3	4	5
1	1	5	2	4	3
2	5	4	1	3	2
3	3	2	4	1	5
4	4	3	5	2	1
5	2	1	3	5	4

Figure 4: Top view of the build plate displaying the Latin square design. The yellow numbers overlaid on the specimens indicate the level of the *Layer no.* factor

of a true in-process condition. In fact, by disabling the up-skin option the last layer will be the same as the one obtained if the printing of a larger specimen was stopped between two consecutive layers. A standard meander scan strategy without contours was used for hatching with a 67-degree rotation between layers.

Table 1: Default process parameters for Ti6Al4V

Slicing parameters		
Layer thickness	60	µm
Hatching parameters		
Number of borders	0	
Hatch distance	95	µm
Rotation btw. layers	67	degrees
Pattern	Meander	
Power	200	W
Exposure time	70	µs
Point distance	60	µm
Up skin parameters		
Up-skin	Disabled	

Down skin parameters		
Down-skin	Enabled	
Skin area tolerance	100	µm
Number of layers	1	-
Replace regular hatches	Yes	
Number of exposures	1	-
Hatch distance (DS)	75	µm
Offset to volume area	-50	µm
Pattern	Meander	
Power	200	W
Exposure time	50	µs
Point distance	80	µm

After printing, all the samples were removed from the build plate by cutting the base supports.

3. Results and discussion

This section describes the methods and procedures employed for off-line surface topography and reconstruction of the internal defects. The extracted results are statistically analyzed and discussed to highlight the effect of the experimental factors.

After removal from the build plate, the specimens were first characterized in terms of surface topography (Section 3.1) and then in terms of internal defects (Section 3.2).

3.1. Topography data analysis

A focus variation microscope, the Alicona Infinite Focus, was chosen for this task thanks to its flexibility in reconstructing large areas with high vertical and lateral resolution. All 25 specimens were measured under the same conditions after removal from the build plate using a vertical and lateral resolution of 1 and 4 µm respectively. Figure 5 shows the topography map of one of the 1-layer specimens after applying an F-operator [19] to remove the expected underlying nominal shape, i.e., a tilted flat surface. A clear distinction between the overhang and bulk regions is visible. The main macroscopic differences are related to higher noise and an apparently lower mean position of the overhang sections w.r.t. supported/bulk regions. In addition, the presence of other, more localized, topographic anomalies should be noted in the bulk-overhang transition region:

- Elongated and deep valleys/voids on the leftmost border of each overhang (Figure 5b): this discontinuity is found approximately at the last down-skin scan line of each overhang (Figure 5c) and it might indicate an unpredictable skipping of 2 or more scan lines by the laser scanner control unit. Another hypothesis is that these voids are due to denudation and subsequent lack of material to melt.

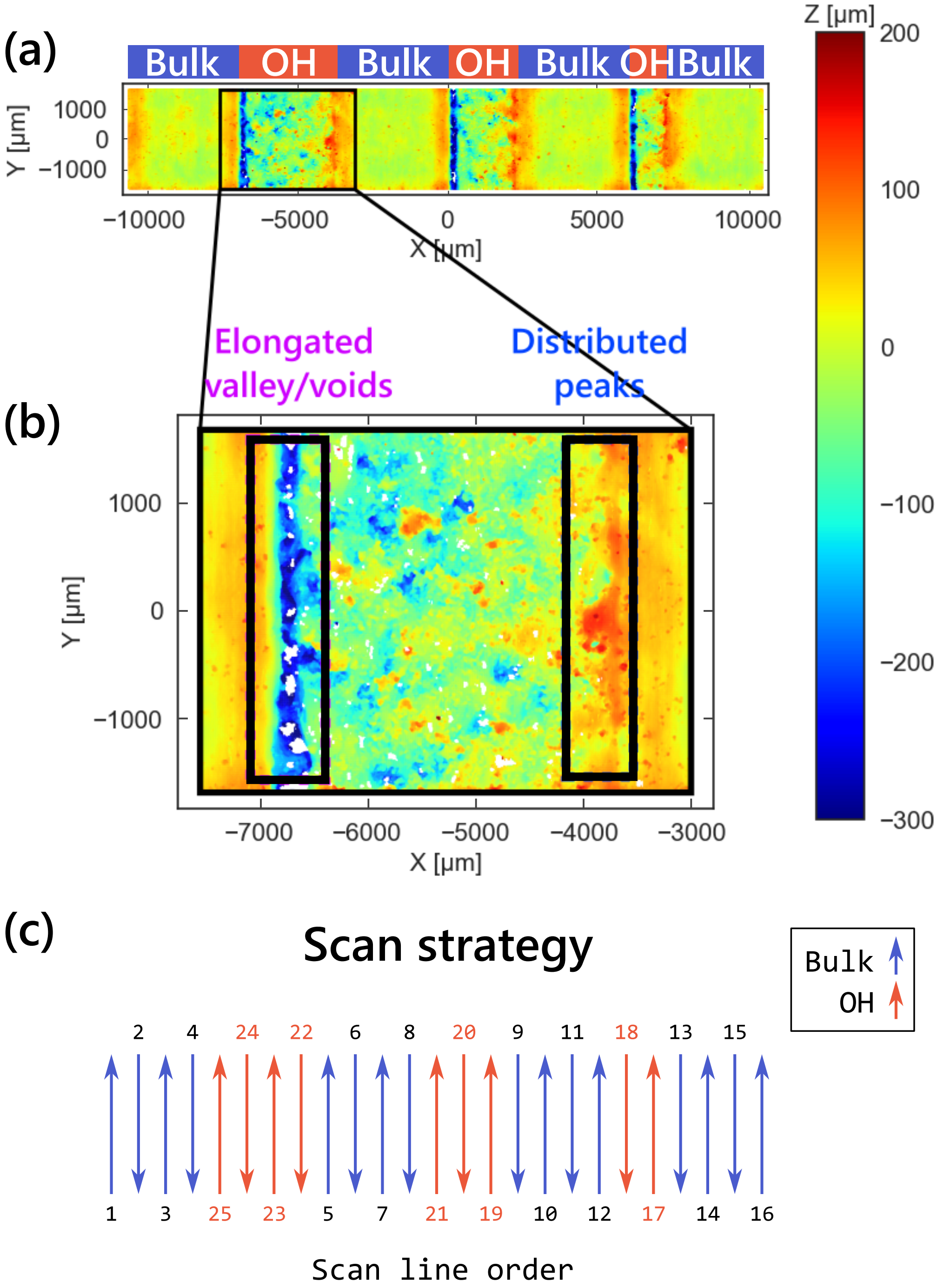

Figure 5: Height map of 1-layer specimen measured via focus variation microscopy. Bulk and overhang regions are highlighted in the top figure (a). The largest overhanging area is enlarged in figure (b) to display the topographic defects in the bulk to overhang transition region. The first overhanging layer scan strategy of the whole sample is displayed in (c).

- Distributed peaks on all the bulk section edges adjacent to the overhang (Figure 5b): these peaks are found in the region where down-skin hatches overlap bulk volume hatches. They can be related to the increased spattering and powder entrapment activity that occurs when laser scans directly on the powder, which is known to create large and irregular particles that fall near the laser track, as investigated by [20].

These anomalies, which are mostly visible after the first overhanging layer, could be also due to the scan strategy employed for the first overhang layer (Figure 5c). The default scan strategy scans the laser over bulk regions before the overhanging sections, potentially creating an undesired discontinuity. The following layers are printed with no distinction between bulk and overhang in terms of process parameters and scan line order.
Nevertheless, all the hypotheses on the formation mechanisms of these localized topographic anomalies would require additional experiments to be verified, possibly using high-speed in-situ monitoring equipment to observe the phenomena. For this reason, elongated valleys and distributed peaks were not studied further in this work.

Surface topography reconstruction provides an information-rich dataset that offers a wide range of possibilities for its analysis: over 100 synthetic indicators [19] for surface texture characterization have been developed over the years to evaluate functional aspects of complex surfaces. Several surface topography indicators have been computed, but they were all found to correlate with each other for the surface under analysis. Therefore, for the statistical analysis in Sections 3.1.1 and 3.1.2, only 2 simple indicators were extracted to describe the evolution of overhang surface topography:

- Average areal height, S_a: this is the 2D extension of the widespread 1D profile parameter R_a (standard definition is reported in ISO 25178 part 2) to evaluate the changes in roughness.
- Relative height, *Z level* (Figure 6): this simple indicator was selected to evaluate the relative surface depression between the overhang and the supported/bulk regions.

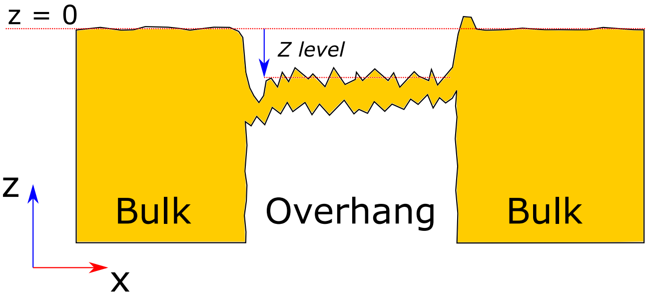

Figure 6: Graphical representation of *Z level* computed after setting to zero the position of bulk surfaces.

A common procedure was developed for the extraction of both variables:

1. *Specimen registration 1*: all specimens were first aligned with a common reference system.
2. *Definition of bulk and overhang evaluation areas (EA)*: the portions of the topographic map that correspond to supported and unsupported regions were selected manually while keeping a sufficiently high margin (≈ 400 µm) from the bulk to overhang transition region to avoid any of the previously identified topographic anomalies. The position and the dimensions of the evaluation areas are shown in Figure 7c.
3. *F-operation*: upon further inspection, all the specimens, especially the 1 and 2-layers ones, showed a slight positive warping of the top surface in the X direction. Since this effect can be traced back to the stress

release after detaching the specimen from the build plate, the deflection was compensated for by fitting a curve via least-squares on the X-Z coordinates of bulk EAs (Figure 7b) and by projecting all points onto the new (curved) reference system.

4. *Specimen registration 2*: the average Z coordinate of bulk EAs was computed for each specimen and subtracted from the whole point cloud to align all specimens with a common reference system (Figure 7c) in Z.

5. *Data extraction*: two different approaches were used for the extraction of the two indicators:

   5.1. *relative height, Z level*: the mean Z coordinate of each overhang EA was computed and extracted;

   5.2. *average areal height,* S_a: a number of evenly spaced circular sampling areas (SA) were defined on the EAs to extract the mean primary surface S_a of each overhang. Since areal characterization standards do not recommend the size or the number of sampling areas to consider and since profilometry standards (ISO 4288) recommend a size (8 mm) and a number (5) of sampling lengths that could not be applied due to the limited extension of the specimen under analysis, the characteristics of the sampling areas were set considering the specific constraints of this application: the sampling area radius was set equal to half the size in the X direction of the smallest EA, which can be rounded to 150 µm. The number of sampling areas was set equal to the maximum number of sampling areas (10) that could be fitted to the smallest EA. The final S_a was then extracted after averaging the 10 roughness values of the SAs.

The values of the extracted parameters are reported in Table B.4.

Together, these two simple indicators give a reasonably complete picture of the sections being studied, providing a quantitative indication of the height distribution of the surface of each section and possible functional effects connected with different height distributions (e.g., localized increase in powder bed thickness, substrate wettability decrease, etc.). Figure 8 shows the probability distribution of the Z coordinate value for three representative levels of *Layer no.* and it was computed using the point clouds of all 3 mm overhang sections ($\approx$ 1 million of points for each histogram, bin size = 10 µm). From Figure 8, it is possible to observe that, due to the combined effect of Z level and surface roughness, the depression can reach more extreme values locally. Localized depressions up to 100-150 µm can be expected in the first OH layer which, combined with the thickness of the next powder layer, can result in a local 200-250 µm thick powder layer, approximately 2-2,5 times the nominal (powder) layer thickness, $lt_{powder,B}$. This local increase affects approximately 20% of the overhang surface, potentially inducing the conditions for the formation of internal defects due to lack-of-fusion, as investigated by Qiu et al. [21].

The main results of statistical analyses performed on the extracted data are reported in the following subsections. Additional details on the models fitted to support the conclusions are reported in Appendix B.

3.1.1. Discussion of S_a data

The surface roughness data are plotted against experimental factors in Figure 9.

The regression analysis performed on all experimental factors, including position factors X and Y, revealed that the S_a measured over bulk sections ($OH\ size = 0$) does depend on the specimen position or the *Layer no.*

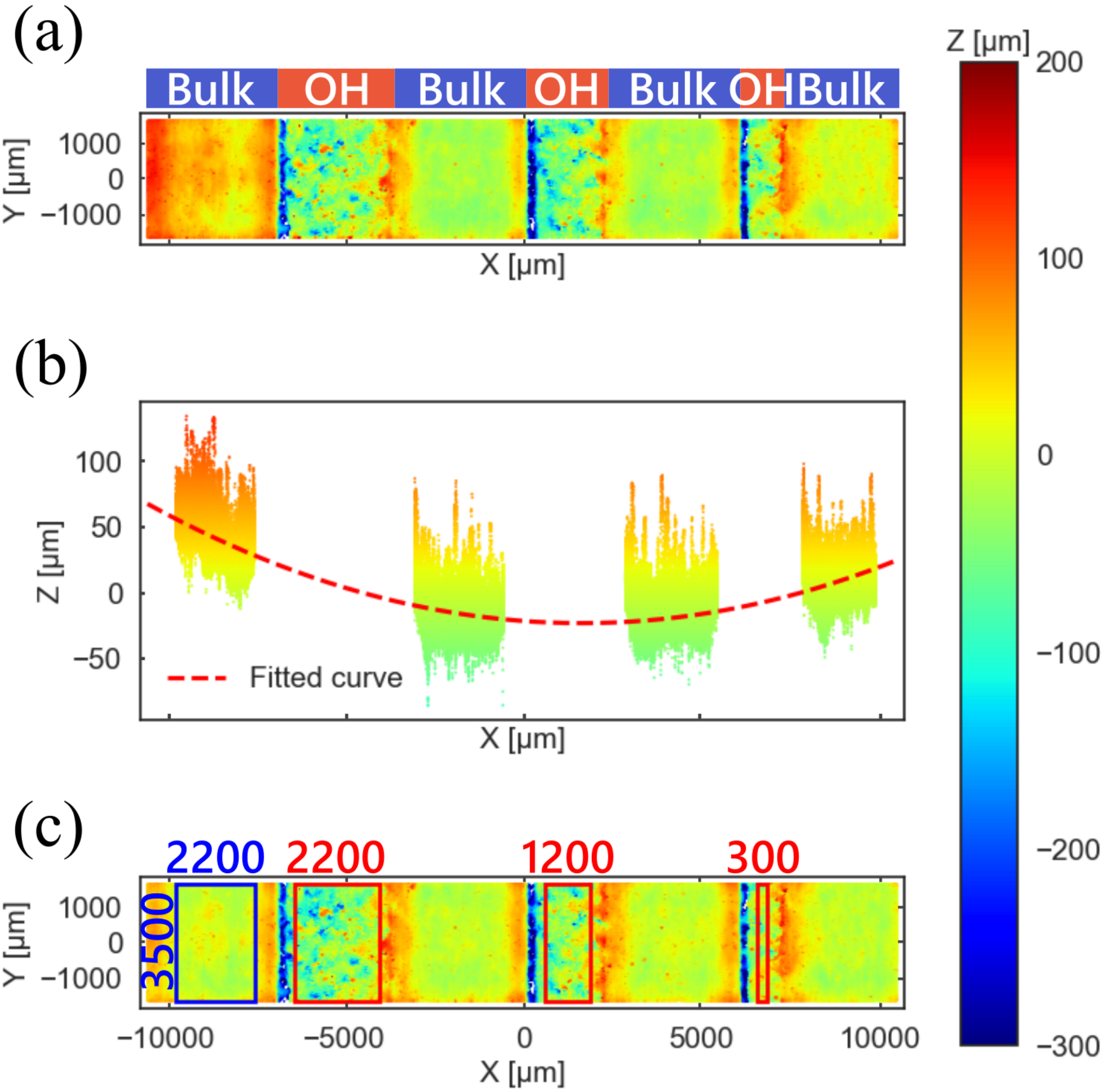

Figure 7: Specimen registration and warp correction. (a) original height map, (b) bulk sections extraction and curve fitting, (c) height map after warp compensation. The evaluation areas of bulk and overhang sections are highlighted in (c).

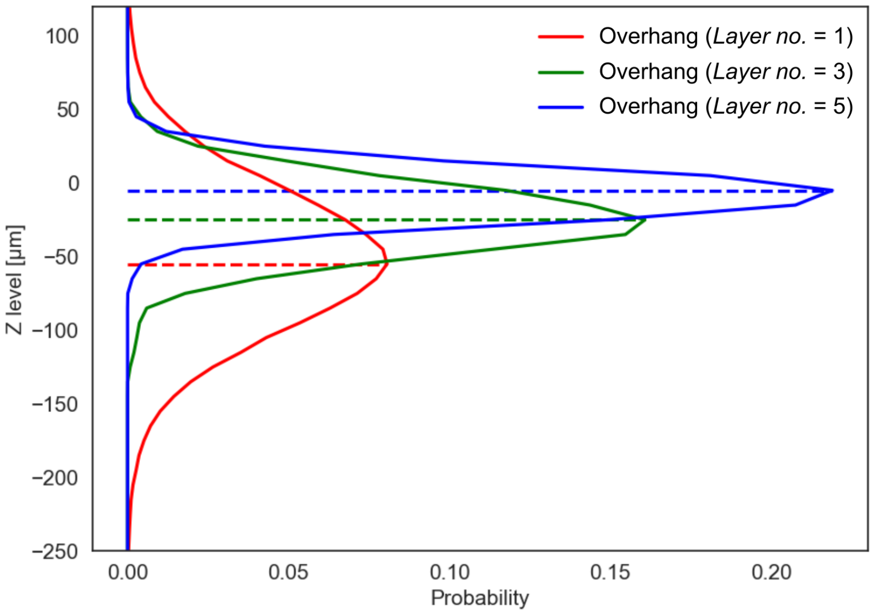

Figure 8: Probability density function of points of different sections

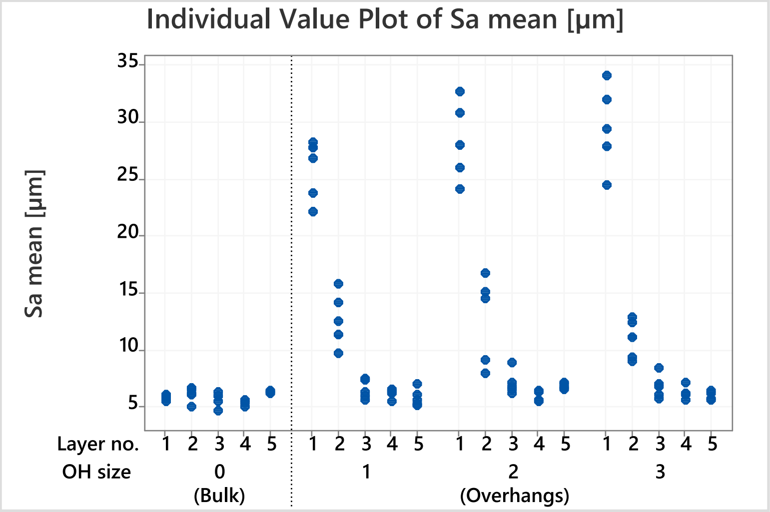

Figure 9: Individual value plots of S_a

This result indicates a well-tuned machine that works in an in-control condition. Since the process is stable over those regions, the values obtained from the analysis of bulk sections can be used to set a baseline to describe the evolution of S_a in overhang regions. From Figure 9 it is possible to observe what seems to be an exponentially decaying trend of S_a against *Layer no.*. The initially high values of the first unsupported layers rapidly decay until they settle around bulk roughness values. A similar decaying trend can be also observed in terms of specimen-to-specimen variance.

Different models were fitted on the remaining data, i.e., *OH size* = 1,2,3, to study the effect of experimental factors on the surface quality of unsupported regions. The results of the analyses offer three main insights on the data:

1. *OH size* factor does not influence significantly the surface roughness. This first result highlights that, in the solidification phase, overhang surface topography is only affected by the type of substrate on which the new layer is printed rather than the extent of the unsupported area.

2. *Layer no.* factor has a significant effect on the surface roughness and the S_a values fit an negative exponential trend very closely.

3. No statistical difference between baseline and the overhang is observed after 3 or more layers are printed. This indicates that, after the third layer, the disturbance introduced by the overhang in terms of substrate roughness is fully recovered.

3.1.2. Discussion of Z level data

The mean depression depth measured using the *Z level* indicator is plotted against experimental levels in Figure 10 and reported in Table B.4. As previously described and shown in Figure 6, the *Z level* values of bulk regions were used for reference setting and will be neglected in the analysis.

Unlike S_a data, which follow a clear exponential trend, *Z level* data are characterized by a higher variability but a trend is visible nonetheless. The depression seems to reduce progressively as new layers are built on top of the unsupported region and becomes negligible after 5 layers. It is also interesting to notice the evolution of the specimen to specimen variability: the depression depths of the first 4 layers after the overhang are characterized by high variability, which seems to drastically reduce at *Layer no.* = 5, thus making the data across the levels of *Layer no.* apparently heteroscedastic.

Different regression models were fitted on the data, and both experimental factors *OH size* and *Layer no.* were found to have a significant effect on *Z level*, specifically:

- The influence of *Layer no.* confirms the trend already observed for S_a data, i.e., any topographic deviation from standard (bulk) surface topography introduced by the overhang is gradually recovered as the process progresses.

- *OH size* shows that the factor plays a significant role in depression formation, probably related to a higher sagging due to the greater extension of the unsupported area.

This last result is in contrast with what was found during the analysis of S_a data and hints that surface roughness and overhang mean depression are governed by two different formation mechanisms. While, as discussed in

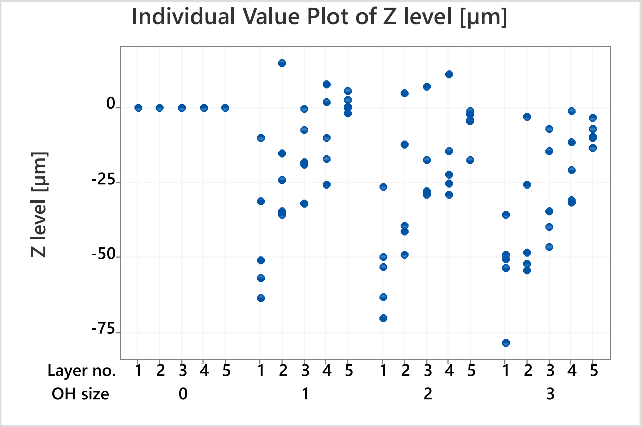

Figure 10: Individual value plot of Z *level*

other publications [22, 23], wettability between the substrate and weld track is considered to be the fundamental physics feature that governs the formation of irregularities in surface topography, excess melting and overheating were found to be the reasons behind the formation of a depression in the overhang sections. The depression depth observed and the melted layer thickness measured by XCT correlates well with the results of a simple model that simulates the effect of powder melting in supported and unsupported regions. The recursive simulation algorithm for computing the depression and layer thickness evolution at the overhang is outlined in Figure 11. The model takes as input the depression depth measured at the first overhanging layer and simulates the effect of melting in the subsequent layers.

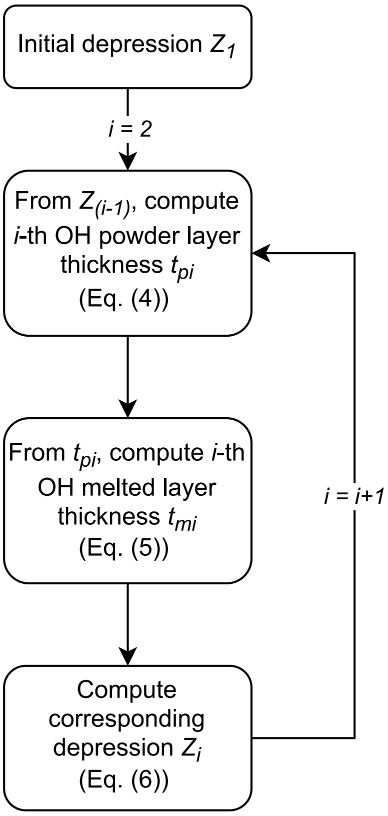

Figure 11: Flowchart for iterative computation of depression depth and layer thickness evolution in the overhang

Figure 12 highlights the evolution of powder and melted layer thicknesses as the process progresses and the resulting depression after printing the i-th layer, Z_i. At each layer, the build plate gets lowered of a predefined amount equal to the layer thickness, lt. When the process is in a steady-state condition, i.e., in correspondence of the bulk sections, the melted thickness at each layer is approximately equal to the predefined layer thickness, lt, and the corresponding nominal powder thickness, lt_p, can be computed as:

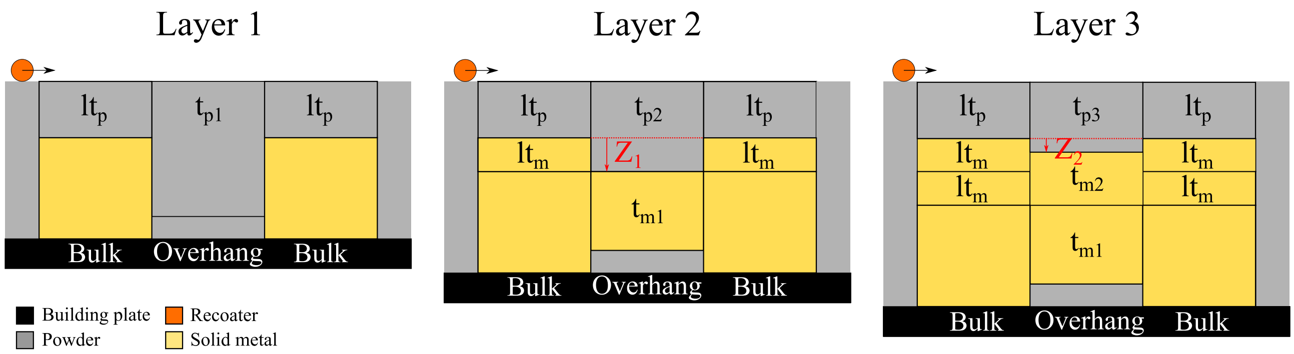

Figure 12: Schematization of the depression formation mechanism due to overmelting in the overhang region

$$lt_p = \frac{lt}{\rho_{rel}} \tag{1}$$

where ρ_{rel} is the relative density of metal powder with respect to solid metal. By taking as input the depression observed after the first layer, Z_1, it is possible to compute the corresponding excess of powder that is melted in correspondence of the overhang for the first layer of powder, t_{p1}:

$$t_{p1} = \frac{Z_1}{1 - \rho_{rel}} + lt_p \tag{2}$$

which corresponds to a melted metal thickness in correspondence of the overhang:

$$t_{m1} = \rho_{rel} t_{p1} \tag{3}$$

The same depression depth of the first overhang layer Z_1 can be used to compute the depression depth and the layer thickness of the generic i-th following layer for both powder, t_pi, and melted, t_mi state following the iterative scheme outlined in Figure 11 and the following equations:

$$t_{pi} = lt_p + Z_{i-1} \tag{4}$$

$$t_{mi} = \rho_{rel} t_{pi} \tag{5}$$

The expected depression depth at layer i will be:

$$Z_i = Z_{i-1} + lt - t_{mi} \tag{6}$$

From the simulation, both depression and overhang layer thickness reduce progressively as new layers are built on top of the unsupported region until the depression becomes negligible and the new layer thickness returns to be approximately equal to the nominal layer thickness, lt. The series of simulated melted thicknesses, t_{mi}, and corresponding depression depths, Z_i, for the first 5 overhang layers ($i = 1, ..., 5$) was computed using an initial depression value $Z_1 = 60$ µm. The results are shown in Figure 13 and compared with measured Z *level* data (Figure 13a) and the mean melt thickness derived from XCT (Figure 13b). The simulated values match the measurements performed on the specimens very closely for both variables, thus confirming the over-melting-related depression formation mechanism.

3.2. Volume analysis

Of all the non-destructive inspection (NDI) techniques for volume reconstruction and internal defect detection, X-ray Computed Tomography (a.k.a. X-ray CT, XCT, or CT) represents the industry standard for inspecting a wide range of parts and materials and it can provide a 3D reconstruction of the region of interest at a high resolution (up to sub-micron resolution).

Volume reconstruction was performed using a micro-XCT scanner made by General Electric (GE), the phoenix v|tome|x m 300kV/500W, and the resolution was set at 10-11 µm per voxel for all acquisitions. After the final reconstruction of the 3D volume of the specimens, the resulting 8-bit greyscale images were exported in a lossless format (TIFF) to perform the next data extraction step.

Although the modest maximum thickness of the specimens and the relatively low density of Ti6Al4V are not critical for tomography, the geometry of the specimen itself, characterized by abrupt changes in thickness and thin overhanging sections, represents a problem for finding the optimal parameter settings for XCT and internal defects detection. In addition, from the analysis of the reconstructed volume, it is possible to observe the composition of the overhang section (Figure 14), which comprises a multi-graded material made up of:

- Solid metal/fully melted powder: high brightness (high density) top region characterized by the presence of pores.
- Sintered powder: lower brightness (lower density) bottom region where single powder grains are visible. From now on, this region will be referred to as *sintered*.

Within the solid and sintered section, several volumetric defects can be detected, i.e.:

- Pores: low brightness, completely surrounded by solid material
- Gaps/voids: these low brightness region appear in the sintered region and between the sintered and the solid metal. Since they cannot be classified as pores, they were not included in the pore count and in the porosity-related indicators discussed in the following subsection.

Due to the inherent differences between the bulk and overhang sections and to the peculiar multi-graded composition of the unsupported regions, a custom segmentation algorithm was developed to reconstruct and study the melted, sintered, and pore volumes separately. The details are reported in Appendix A.

3.2.1. Tomography data extraction

The high-resolution 3D reconstruction combined with the segmentation algorithm developed made it possible to identify and quantify interesting response variables related to the melted and the sintered fraction. The following representative variables were chosen for the analysis:

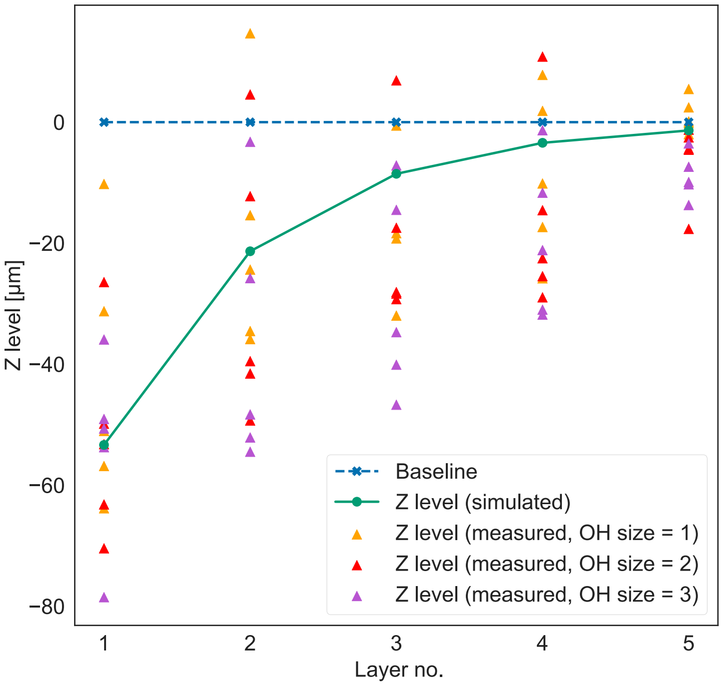

(a) Simulated depression depth against measured *Z level*

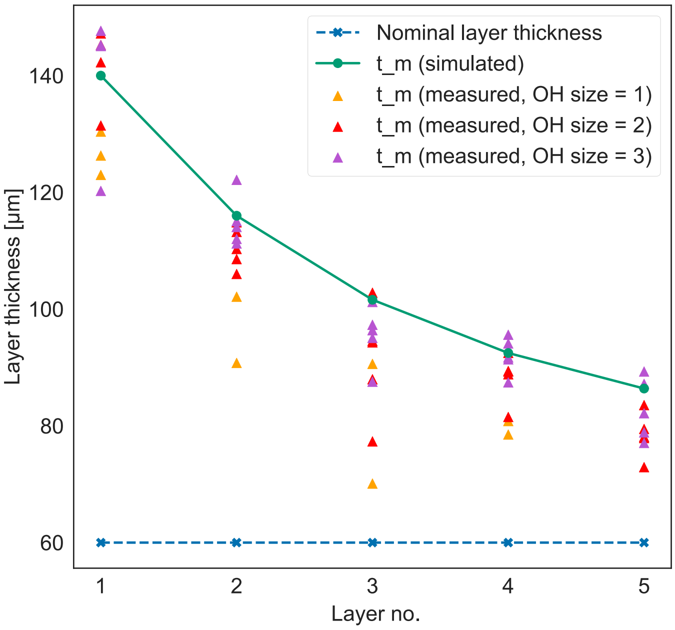

(b) Simulated melted layer thickness against measured data from XCT (see Section 3.2.1 for details on the computation)

Figure 13: Simulation results against experimental results on overhang depression formation

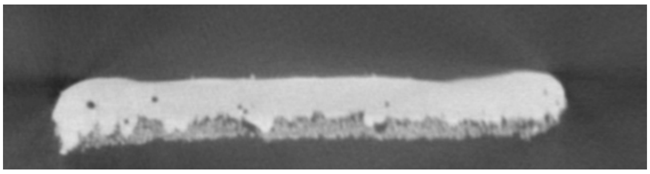

Figure 14: Sample XCT reconstructed slice (YZ plane) of the overhang

- Equivalent melted layer thickness in the overhang, t_m [µm]

$$t_m = \frac{V_m}{A * Layer\ no.} \tag{7}$$

where V_m is the melted volume and A is the areal extension of the corresponding overhang

- Equivalent sintered thickness in the overhang, t_s [µm]

$$t_s = \frac{V_s}{A} \tag{8}$$

where V_s is the sintered volume in correspondence of the overhang

- Density, ρ [%]

$$\rho = \frac{V_m}{V_m + V_{pores}} \tag{9}$$

where V_{pores} is the pores volume

- pore density, ρ_{pores} [mm^{-3}]

$$\rho_{pores} = \frac{Pores\ no.}{V_m} \tag{10}$$

All the data is reported in Table **??** and B.9. To compute these response variables, a procedure similar to that already described in Section 3.1 was created to extract the number of pores and all the volume-related data:

1. *Specimens registration*: all specimens were aligned with respect to a common reference system

2. *Definition of bulk and overhangs evaluation volumes (EV)*: the sections of the XCT that correspond to supported and unsupported regions were selected manually. Due to beam hardening artifacts produced by the abrupt change in thickness, approximately 10 slices from each bulk to overhang transition regions were discarded from the analysis. The position and the dimensions of the evaluation volumes are reported in Figure 15.

3. *Segmentation*: segmentation was performed by applying the method developed in Appendix A on the slices of each evaluation volume.

4. *Pores filtering*: before extracting any porosity-related quantity, a filter was applied to discard pores smaller than $2 \times 2 \times 2$ voxels, which, considering the 11 µm resolution used for all acquisitions, corresponds to an equivalent diameter of ≈ 27 µm.

5. *Data extraction*: the following raw values were extracted:

    - melted volume, V_m
    - sintered volume, V_s
    - pores volume, V_{pores}
    - pores number, $Pores\ no.$

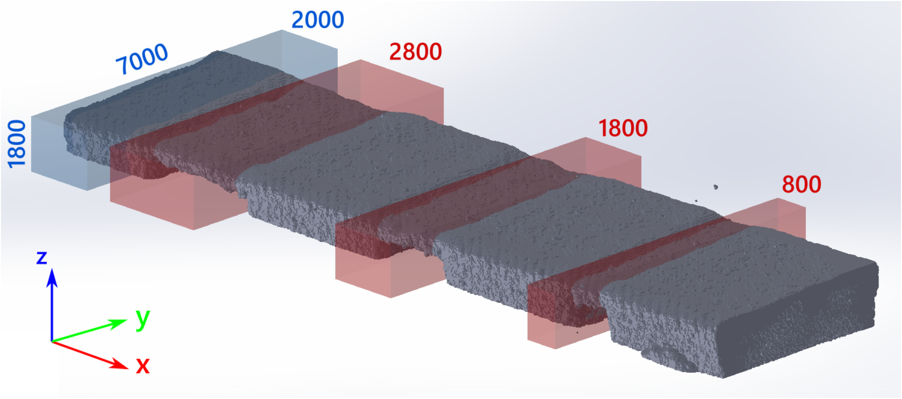

Figure 15: The evaluation volumes of each section are overlayed on top of the reconstructed volume. The bulk EV is shown in blue while the 3 overhangs EVs are shown in red. Y and Z dimensions of all EVs are kept constant. All sizes are in µm

Before analyzing and discussing the results, it should be pointed out that a small number of observations are missing for the *OH size* = 1 level due to small misalignments in the acquisition phase that led to the production of partial volume artifacts at the smaller overhang. Table 2 summarizes the number of observations acquired for each combination of the experimental factors out of the 5 replicas that were built.

Table 2: Treatments analyzed via XCT scanning

		OH size			
		0 (bulk)	**1 (5 mm^2)**	**2 (10 mm^2)**	**3 (15 mm^2)**
Layer no.	**1**	4	3	4	4
	2	5	3	5	5
	3	5	2	5	5
	4	5	2	5	5
	5	5	0	5	5

3.2.2. Discussion on melted and sintered thickness

In Figure 16 all the thickness-related variables are plotted against the two experimental factors, *OH size* and *Layer no.* Despite not being related to internal defects, the regression analyses performed on the equivalent melted layer, t_m, and sintered thicknesses, t_s, computed from V_m and V_s respectively, offer quantitative insights on how the layer thickness progresses at the overhang and on the factors that affect the formation of sintered powder. Both contribute to the dimensional and geometrical accuracy of the overhang and, as far as cleanliness is concerned, it is important to keep the amount of sintered powder created for different overhang extensions under control. The fitted regression models reveal that all experimental factors strongly influence the thickness values. The melted thickness t_m shows significantly higher values in the first layers, thus indicating that a thicker layer of powder gets melted in the first layer of the overhang due to over-melting and that the following layers gradually recover from this deviation in layer thickness. This result is in agreement with the thickness layer progression simulated in Section 3.1.2 and confirms the depression formation mechanism due to over-melting. Interestingly, the melted thickness is also affected by the *OH size*, probably suggesting that larger overhangs create a more severe heat accumulation in that area, thus leading to a higher volume of powder getting melted.

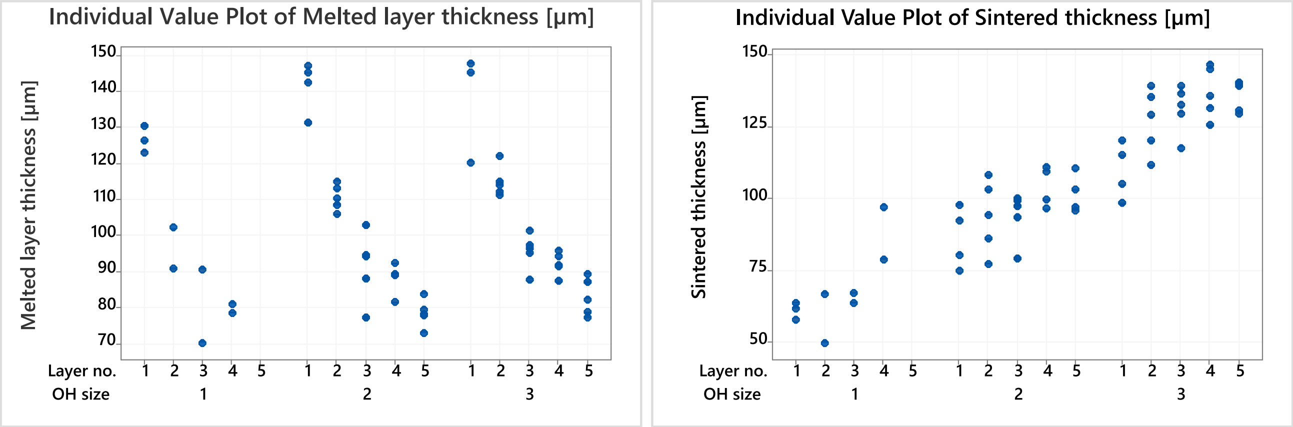

(a) *Equivalent melted thickness,* t_m

(b) *Equivalent sintered thickness,* t_s

Figure 16: Individual Value Plots of thickness-related variables

A similar mechanism is assumed to influence t_s, which was found to be significantly affected by the size of the overhang and, to a lesser extent, by the number of layers. However, the positive linear dependency of t_s on *Layer no.* is expected to be valid only within the short layer span studied in this experiment. The sintered thickness should reach a maximum once the new layer's heat input is sufficiently far away and no longer contributes to increasing the amount of sintered powder in the down-skin region. In terms of values, it should be noted that this secondary effect of powder melting has resulted in an equivalent thickness that ranges from 1 to 2,5 times the nominal layer thickness, depending on the extension of the down-facing surface. These values require great attention in the post-processing phase if the part is designed to work in a cleanliness-sensitive environment.

3.2.3. Discussion on internal defects

In Figure 17 all the thickness-related variables are plotted against the two experimental factors, *OH size* and *Layer no.*

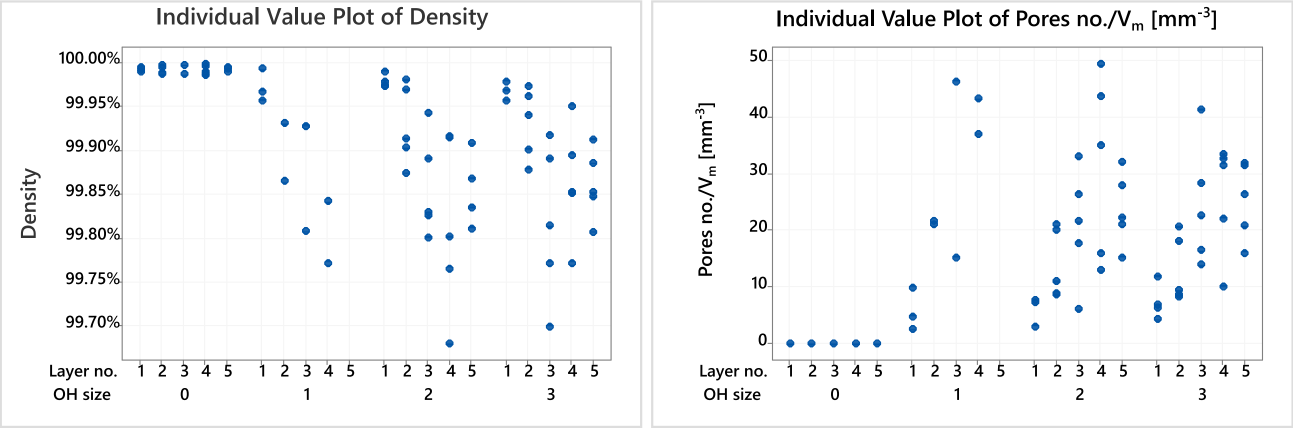

(a) *Density,* ρ

(b) *Pore density,* ρ_{pores}

Figure 17: Individual Value Plots of porosity-related variables

The structure of internal defects and their trends in relation to the experimental factors were captured by the values of density, ρ, and pore density, ρ_{pores}. Both indicators were extracted to provide a thorough description of the internal defects but, as far as this experiment is concerned, a very high linear correlation was found between the two. For this reason, only the pore density data was studied in-depth since the other indicator does not provide any additional insights on the structure of the internal defects.

From the plot in Figure 17b, it is possible to observe that the bulk sections ($OH\ size = 0$) analyzed in the specimens are almost free of pores, indicating an in-control process when standard process parameters are used and the geometry does not comprise complex features. On the other hand, overhang sections display a much more complex internal defects structure which does not seem to be significantly influenced by the size of the overhang. Very few pores are detected in 1-layer specimens but the pores structure changes when other layers are added, resulting in a lower density and a higher specimen to specimen variability. A regression model was fitted to study the peculiar pattern found in the unsupported regions. ANOVA shows that *OH size* does not affect ρ_{pores} and highlights a second-order dependence on *Layer no.* (Table 3).

Table 3: ANOVA table on pore density data

Source	DF	Adj SS	F-Value	P-Value
Regression	3	4018.9	17.07	0.000
OH size	1	184	2.34	0.132
Layer no.	1	1448.2	18.46	0.000
Layer no.^{2}	1	741.9	9.46	0.003
Error	53	4158.3		
Lack-of-Fit	10	588.4	0.71	0.711
Pure Error	43	3569.9		
Total	56	8177.2		

The significance of the second-order term seems to hint that, even though not observed in full within the studied experimental range, pore density starts to decrease after hitting a maximum after 3-4 layers (Figure 18). The quadratic trend seems to correlate well also with the specimen-to-specimen variability: the lower the pore density, the higher the variability. This reflects the highly stochastic nature of pore formation in the overhang region. Despite the peculiar trend followed by the pore density values in the overhang region, it should be pointed out that the overall density never dropped below 99.5% in any of the regions studied, which is often

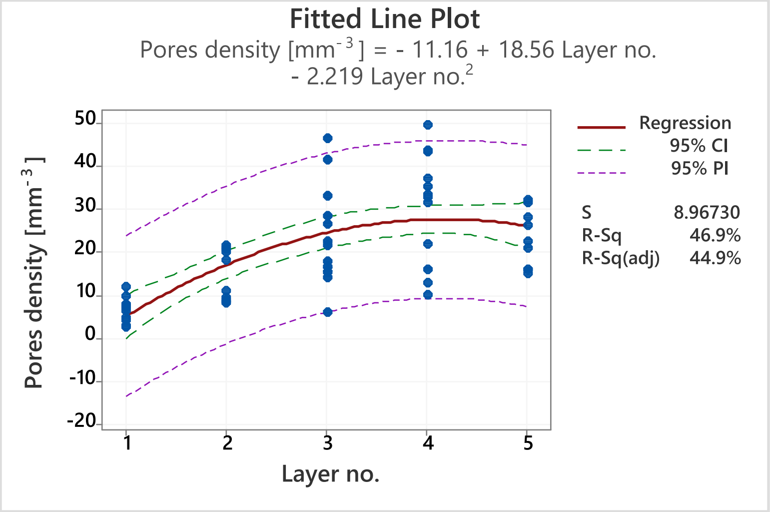

Figure 18: Regression model on ρ_{pores}

considered the industry standard for as-built AM parts. However, being a global indicator, its high values do not necessarily correspond to a uniform pores distribution within the specimen.

To further investigate the formation of internal defects, specimens were aligned with respect to a common reference system, and the pore distribution along the Z coordinate in the 3 mm overhang ($OH\ size = 3$) were plotted for each *Layer no.* level (see Figure 19, bin size = 25 µm). Each subplot displays:

- Pore distribution found in the samples built with a specific *Layer no.* level (black dots).
- Size (thickness) and position of every single layer built up to that point. Single layers are shown as colored rectangles built on top of each other (Layer 1 = purple, Layer 2 = red, etc.). The equivalent layer thickness was computed from the melted thickness t_m data.

It should be noted that the sharp borders shown in the plot do not correspond to reality as the top and bottom surfaces of each overhang are characterized by irregular profiles which may include other pores. For this reason, a few "dots" of the pore distribution appear outside of the colored areas that represent each single layer.

The porosity evolution shown in Figure 19 confirms the trend observed with the synthetic density indicator, but it also offers some additional insights that allow us to trace back the origin of pores and to understand more about their formation mechanism. Looking at the subplots in Figure 19, it is possible to observe that when a new layer is printed, the newly added melted material is almost pores free, but, as the process progresses, new pores are seeded in the area of the previously fully dense layers. For example, the third printed layer in the third subplot (green rectangle) is almost fully dense, but its addition creates a significant increase in the number of pores in correspondence of the first layer (purple rectangle).

This mechanism reveals that most pores develop within previously solidified layers, i.e., during remelting due to the addition of a new layer. This effect is usually caused by the presence of an unstable melting condition, called keyhole. The keyhole usually forms when the energy density is too high or in presence of geometry-induced overheating [25], which is the expected condition when printing overhangs. Under this melting mode, an unstable vapor-filled depression forms and it may give origin to trapped metal vapor pores at the bottom of the keyhole, as described in [24]. Since the keyhole height usually spans several layer thicknesses, it could induce a "pore seeding" mechanism in the previous layers. Most pores, in fact, appear near the bottom surface only after the third layer is printed. This keyhole porosity mechanism seems to also affect the process when layers 4 and 5 are printed, as new pores are seeded in the second and third layer as well. However, the number of pores generated in correspondence of the second and third layer seems to become progressively smaller, possibly indicating that the unstable keyhole conditions are not quite as frequent as the process moves farther away from the overhang and heat dissipates more efficiently.

4. Conclusions

The proposed strategy of interrupting the printing process after a variable number of layers from the start of the overhang enabled ex-situ analysis of specimens representative of different process phases. It also allowed us to study the evolution of effects induced by the presence of overhanging surfaces with the accuracy of off-line equipment. Furthermore, the evolution of surface topography and printed volume was quantitatively investigated in this study to understand defect formation mechanisms and how they are affected by the areal extension of the

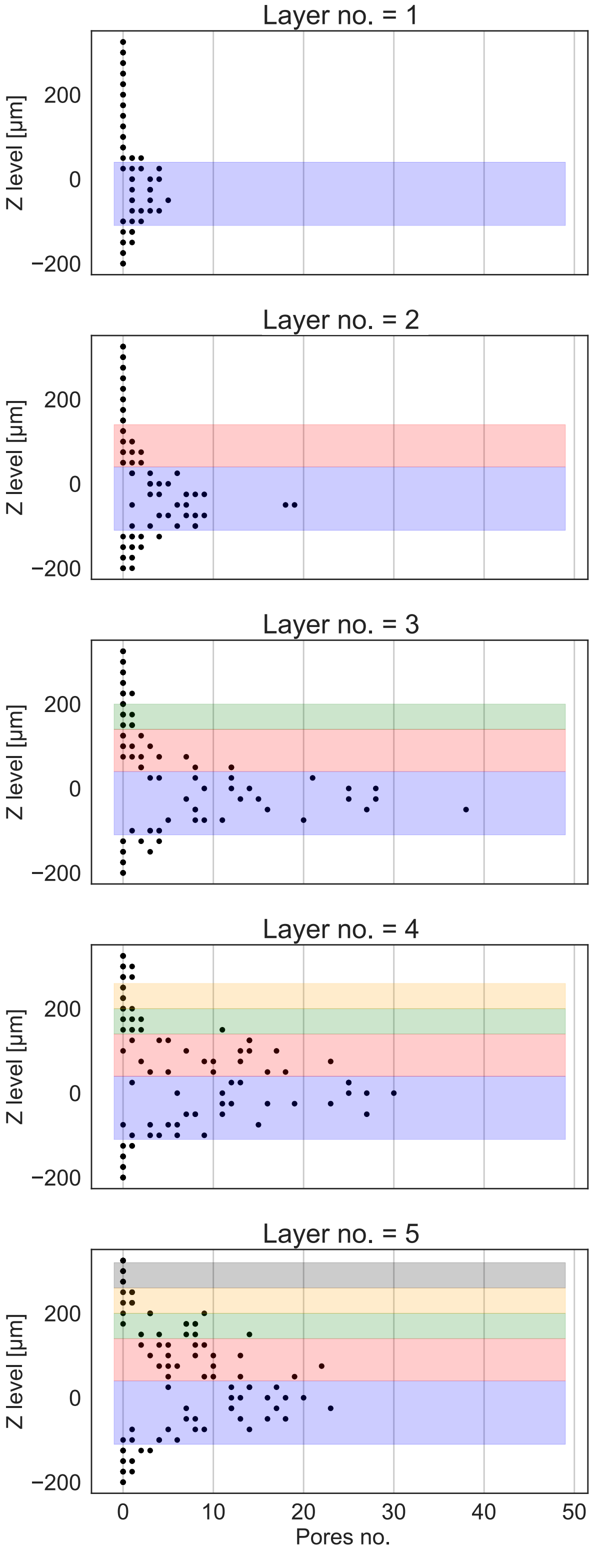

Figure 19: Pores distribution along Z in the 3 mm overhang of all analyzed specimens. The colored areas represent the location of each of the 5 layers as they are added during the print.

overhanging surface as the process progresses. The experimental setting analyzed in this work is representative of an industry-standard condition, but it still refers to a specific machine-material-process parameters combination. Future work will aim at verifying the validity of all results and models for different experimental settings.

Surface characteristics were studied in terms of roughness, S_a, and depression formation, *Z level*, and they were found to be significantly affected by the presence of unsupported areas. However, the process can be considered stable as deviations from the steady-state in terms of surface topography tend to be recovered within a relatively short process span, i.e. after 3-5 layers. On the other hand, it was found that the extension of the overhang does not affect S_a and has a minor influence on the *Z level* data. This result highlights that overhang surface topography is mostly affected by the type of substrate on which the overhang is printed, i.e. powder. This makes any unsupported area potentially critical for the development of irregular surface topography which, as discussed in the previous sections, can result in a significant local increase in the powder thickness (up to 2,5 times the nominal layer thickness).

Other topographic anomalies, i.e., elongated valleys and distributed peaks, were detected especially in the bulk-overhang transition regions. Few hypotheses have been formulated on their formation mechanisms and they will be investigated further in future work using in-process high-speed monitoring together with laser scanner position probing.

To understand the underlying mechanism of surface depression formation at the overhang, a recursive analytical model was developed to simulate depression progression given an initial depression value. In addition, the model makes it possible to compute the effective powder and melted thickness for each layer at the overhang and can be used to predict dimensional errors.

Volume analysis using high-resolution XCT made it possible to capture the porosity structure and the multi-density composition of overhang sections, which are composed of fully melted and sintered powder. A new segmentation algorithm was developed to correctly reconstruct and divide the two regions to analyze them separately. This made it possible to study the evolution of the melted thickness (t_m) and provided validation of the analytical model developed to predict the evolution of surface depression at the overhang due to over melting.

The sintered thickness (t_s) was also computed from the reconstructed XCT volume and it was found to have a positive linear relationship with the areal extension of the overhang due to the increased heat accumulation of larger unsupported areas. The values of sintered thickness can reach up to 2,5 times lt in the as-built conditions, which makes it potentially critical if the part is designed to work in a cleanliness sensitive environment and if surface finishing treatments cannot be employed (e.g., inaccessible surface due to complex geometry).

The pore density found in the fully-melted fraction of the unsupported region revealed that the local density in the overhang region is lower than bulk density. However, the overhang size was not found to influence the resulting pore density, thus confirming that all overhanging surfaces above 5 mm^2 will present a similar density structure. The results, however, do not seem to correlate with surface topography indicators, indicating that the unfavorable printing conditions detected during the surface topography analysis did not affect pores formation. To understand the fundamental mechanism of formation that results in the peculiar porosity evolution reconstructed using XCT, the location of the overhang pores was investigated. This final analysis allowed us to shed light on the pores formation mechanism, which was found to be mostly related to remelting and unstable keyhole formation. The pores distribution in the overhang highlighted a non-uniform pore density across the overhang thickness. In addition, a high pore concentration was detected near the down-skin, which will result in a local density lower than the industry standard of 99.5%.

All the results indicate that, near the down-facing surface of flat overhangs, volumetric defects (pores), dimensional errors (increased melted and sintered thickness), and in-process deviations from standard substrate surface quality (higher roughness and depression formation) can be expected. The higher concentration of pores and the presence of sintered powder can be particularly detrimental for the final part quality, and in-process deviations from standard substrate surface are potentially critical for the process. The key findings of this work convert into three major implications for dealing with parts that contain overhangs. These comprise already applicable design guidelines and possible research paths that need to be explored in the future:

1. *Stock allowance*: the disturbance effect introduced by the overhang – in terms of surface topography and internal defects – mostly affects the first 4-5 overhang layers. This value can help defining the minimum excess material that should be added to the initial design and removed via post-processing to avoid potentially critical layers in the final part (i.e., those containing a higher concentration of volume defects or that have been printed over a lower quality substrate).

2. *In-situ monitoring and control*: the surface topography results indicate that surface roughness and out-of-plane defects, i.e. surface depression, could be measured in-situ to indirectly evaluate the quality of overhangs during the process and to develop a process control strategy to recover from the topography deviations.

3. *Process parameters optimization*: current default process parameters adopt a modified printing profile only for the first overhang layer, while the following are printed with bulk parameters. Future work will be devoted to process parameters optimization across all the first overhang layers to:
    - Improve dimensional and geometrical accuracy in the overhang
    - reduce the formation of sintered thickness
    - reduce pore formation due to overheating and keyhole melting.

5. Declarations

5.1. Funding

This project was partially funded by ESA (Contract No. 4000125528/18/NL/MH/mg) and RUAG in the frame of Matteo Bugatti's co-sponsored Ph.D.

5.2. Competing interest

The authors declare that they have no known competing financial interests or personal relationships that could have appeared to influence the work reported in this paper.

5.3. Availability

Processed data are available in Appendix B. The raw data required to reproduce these findings cannot be shared at this time due to technical or time limitations.

5.4. Code availability

The code used to reproduce these findings cannot be shared at this time due to technical or time limitations.

5.5. Ethics approval

Not applicable.

5.6. Authors' contributions

M.B. and B.M.C. conceived the experiment. M.B. conducted the L-PBF experiment and performed the characterization on the specimens. M.B. and Q.S. developed the statistical and analytical models. M.B. was involved in drafting the manuscript and Q.S. and B.M.C. in revising it critically for important intellectual content. All the authors contributed to and read the final manuscript.

Appendix A. Segmentation algorithm

Image segmentation represents a fundamental branch of image processing and it makes it possible to automatically divide the image into meaningful segments or parts for further quantitative analysis. To complete this task, different approaches can be implemented. A detailed description of the traditional image processing methods, together with a discussion of the pros, cons, and applicability can be found elsewhere [26, 27].
Arguably, the simplest methods for image segmentation are thresholding-based techniques. These approaches are used to split image pixels into categories depending on their intensity level and, in general, they perform well when there is good separation between different regions of the image in terms of grey-scale level and when the number of clusters in the image is known *a priori*. These two conditions are usually met when performing segmentation of XCT images of mechanical components, where only binarization must be performed (2 clusters) and the grey levels of background and part are well separated. However, as discussed in 3.2, the composition of the overhang slices makes it impossible to reconstruct the internal defects by applying standard binarization techniques (e.g. the thresholding method developed by [28]). If the correct number of clusters is not considered, the dual-phase nature of the overhang section is disregarded, thus resulting in a segmentation that merges the sintered fraction with either the background or the melted powder and where most of the reconstructed internal defects are the larger gaps in the sintered region (Figure A.20c).

Assuming an approximately normal distribution of the intensities of pixels that belong to different regions, a Gaussian mixture model (GMM) was fitted to two representative XCT slice image histograms of the bulk and overhang regions.
Figure A.21 shows the histogram of a typical bulk section: even if the pixel count does not fit a normal distribution tightly, a clear separation between low and high level intensity pixels, which define the background and melted regions respectively, is visible, suggesting the application of 2 cluster segmentation.

On the other hand, the XCT images of overhang regions show a histogram that is more difficult to interpret, as an additional distribution between solid and background seems to be present. In Figure A.22, 2 and 3 cluster GMM models are overlaid on top of the image histogram in Figure 14: when only 2 clusters are set, the low-intensity peak that corresponds to the background is correctly identified, but for the high-intensity values a very broad distribution is fitted to cover the two peaks that correspond to sintered and melted regions

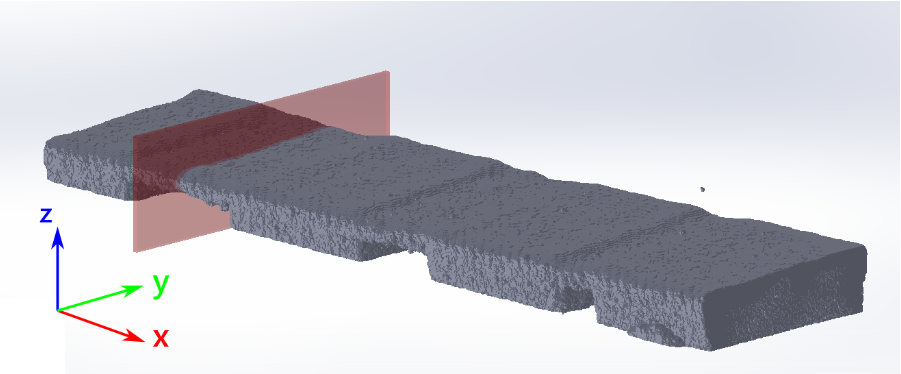

(a) Slice position

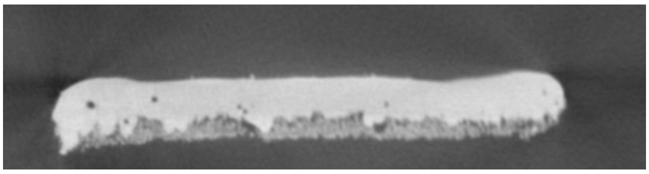

(b) Original overhang slice

(c) Slice after binarization with Otsu method

Figure A.20: Example of overhang slice with multi-graded density and resulting binarization with Otsu method

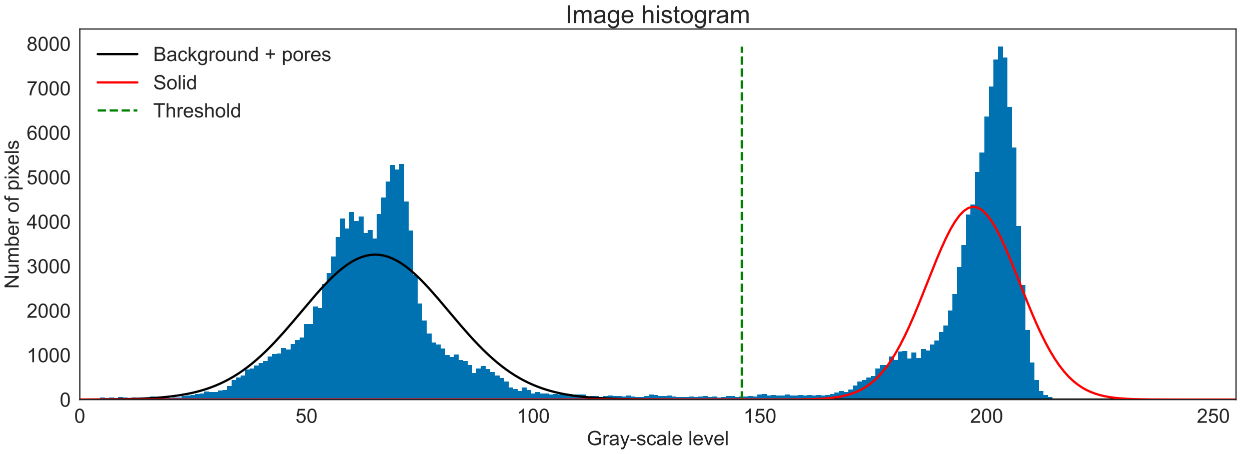

Figure A.21: Histogram of a bulk region slice (Figure A.23a) respectively. The single threshold neglects the difference between low and high density in the overhang, resulting in the poor segmentation performance of Figure A.20c. With 3-clusters the fitted GMM reflects the underlying histogram more closely and it makes it possible to define an additional threshold that partitions the image into 3 sections.

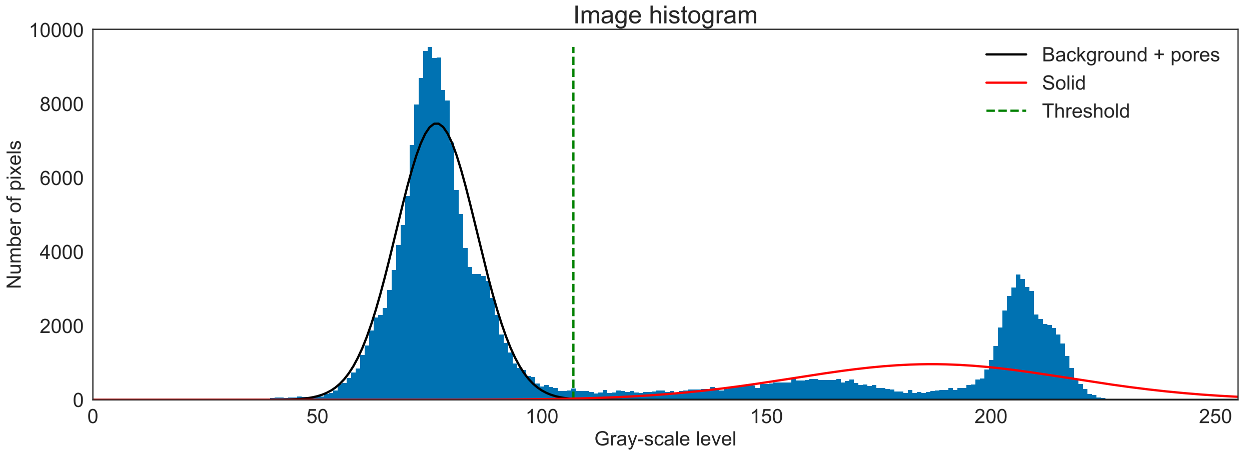

(a) Histogram of an overhang region slice with 2 fitted clusters

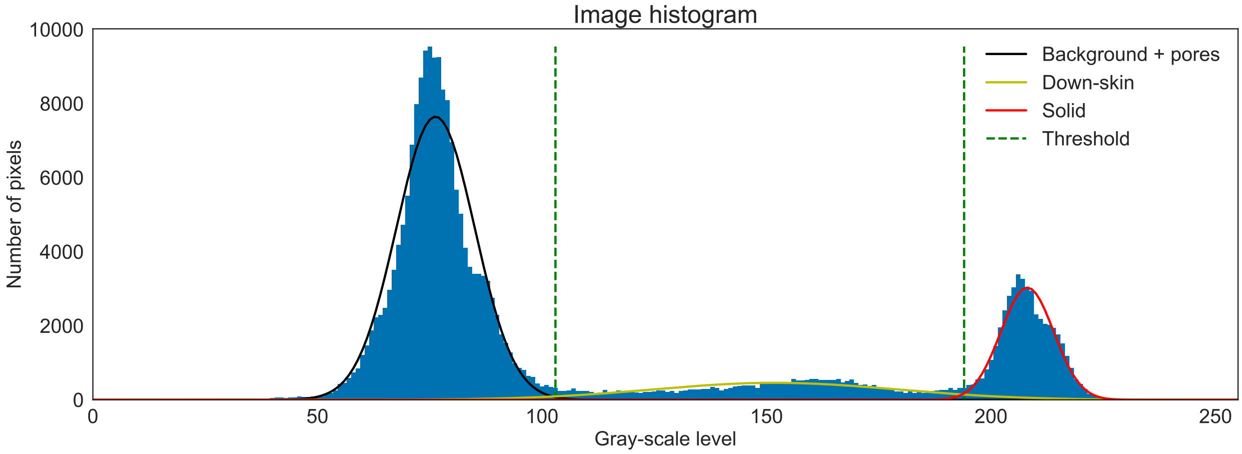

(b) Histogram of an overhang region slice with 3 fitted clusters

Figure A.22: Histogram of Figure A.20b with 2 and 3 clusters

Thanks to the satisfactory performance obtained with the simple multi-cluster extension of the threshold-based clustering method, all slices were segmented using the Otsu method and the number of clusters for each slice was selected, according to their position in the image stack, as either 2 clusters (for bulk) or 3 clusters (for overhang sections). Figures A.23 and A.24 show two sample images of bulk and overhang regions before and after segmentation with the optimal number of clusters.

As shown in the figure, thanks to the additional cluster the sintered and melted regions could be separated into two different sections of the image: this result represents a significant improvement over the binarization of Figure A.20c and it also allowed us to reconstruct smaller pores in the melted fraction thanks to the higher additional threshold.

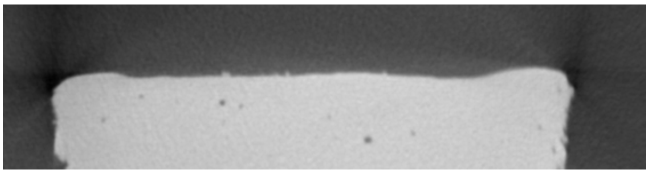

(a) Original image

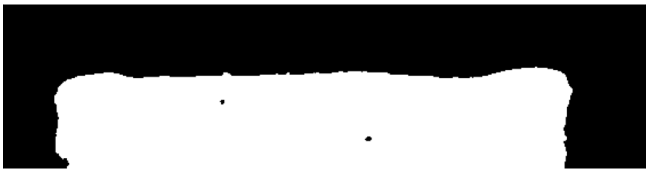

(b) Otsu segmentation with 2 clusters

Figure A.23: Bulk slice segmentation

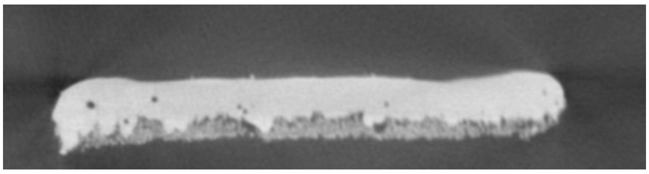

(a) Original image

(b) Otsu segmentation with 3 clusters

Figure A.24: Overhang slice segmentation

Appendix B. Datasets and statistical analyses

All the data and additional details on the statistical analyses discussed in Sections 3.1 and 3.2 are reported in this Appendix. Please note that all the statistical models, unless otherwise specified, can be considered valid only for the specific machine-material-parameters combination used in this experimental setting.

Appendix B.1. Topography data and statistical analyses

The results extracted from the surface maps (Section 3.1) are shown in Table B.4. The details of the statistical analyses are reported in the following subsections.

Appendix B.1.1. Details on the statistical analysis of S_a

The resuls of the first preliminary analysis on the bulk sections ($OH\ size = 0$) to evaluate the effect of the *Layer no.* factor and blocking factors X and Y are shown in Table B.5.

At a 5% significance level ($\alpha = 0.05$), none of the studied factors affects the substrate surface roughness of supported bulk regions, confirming that the position of the specimen does not interact with the process, at least in terms of surface roughness, indicating a well-tuned machine.

The ANOVA on the remaining set of S_a data ($OH\ size = 1{,}2{,}3$) was performed after natural log transformation to recover homoscedasticity (Box-Cox power transformation, $\lambda = 0$) and revealed that the size of the overhang does not significantly influence surface roughness (Table B.6): this first result highlights that, in the solidification phase, overhang surface topography is only affected by the type of substrate on which the new layer is printed rather than the extent of the unsupported area. On the other hand, *Layer no.* was found to affect the response with an exponential trend which was used to fit a regression model.

To deal with the heteroscedasticity across different treatments, the final regression model was fitted after applying a natural log transformation to the data and using $exp(-Layer\ no.)$ as a regressor to model the exponentially decaying trend, as shown in:

$$\ln(S_a) = 1.764 + 4.321 * exp(-Layer\ no.) \tag{B.1}$$

The results obtained with model (B.1) are shown in Figure B.25 Pairwise comparison was then performed between *Layer no.* levels to quantify the number of layers required to get back to steady-state surface topography. The results (Table B.7) show no statistical difference between baseline and the overhang after 3 or more layers are printed, indicating that, after the third layer, the disturbance introduced by the overhang in terms of substrate roughness is fully recovered.

Appendix B.1.2. Details on the statistical analysis of Z level

The model and ANOVA table of the regression analysis discussed in Section 3.1.2 is shown here. A satisfactory model fit was obtained with a simple linear function using *Layer no.* and *OH size* levels as regressors:

$$Z\ level = -42.00 + 10.30 * Layer\ no. - 6.25 * OH\ size \tag{B.2}$$

Table B.4: Extracted data from surface topography reconstruction

				OH size							
				0		**1**		**2**		**3**	
Specimen no.	**X**	**Y**	**Layer no.**	**Z level [µm]**	**Sa [µm]**	**Z level [µm]**	**Sa [µm]**	**Z level [µm]**	**Sa [µm]**	**Z level [µm]**	**Sa [µm]**
11	1	1	1	0.00	6.06	-10.22	23.78	-26.43	24.16	-35.92	27.86
21	3	2		0.00	5.73	-56.82	22.13	-53.21	25.95	-50.64	24.47
31	4	3		0.00	5.45	-63.81	27.78	-63.17	32.65	-78.50	29.35
41	5	4		0.00	5.52	-51.02	26.80	-70.42	30.85	-53.72	34.08
51	2	5		0.00	5.95	-31.25	28.24	-49.83	28.04	-49.05	32.03
12	3	1	2	0.00	6.55	-15.39	14.14	-12.24	16.69	-25.78	12.90
22	5	2		0.00	6.06	14.67	12.51	4.57	9.17	-3.25	9.06
32	2	3		0.00	6.71	-35.85	9.72	-49.30	14.56	-48.30	9.31
42	4	4		0.00	5.07	-34.52	11.39	-39.50	15.08	-54.47	11.14
52	1	5		0.00	6.20	-24.36	15.79	-41.54	7.98	-52.11	12.34
13	5	1	3	0.00	5.49	-7.66	5.56	6.90	6.75	-7.16	5.73
23	4	2		0.00	4.67	-0.56	6.31	-17.45	6.54	-14.49	6.06
33	1	3		0.00	6.31	-18.36	7.37	-28.33	7.16	-34.71	7.00
43	2	4		0.00	6.00	-31.96	7.49	-28.08	8.84	-40.08	6.73
53	3	5		0.00	5.50	-19.22	5.95	-29.25	6.22	-46.70	8.46
14	4	1	4	0.00	5.59	1.87	6.26	10.83	5.44	-1.34	6.19
24	2	2		0.00	5.01	7.81	6.58	-14.55	5.58	-21.14	5.63
34	3	3		0.00	5.62	-25.81	6.19	-28.95	5.64	-30.98	6.03
44	1	4		0.00	5.63	-10.14	5.42	-22.50	6.26	-11.66	6.18
54	5	5		0.00	5.32	-17.33	6.43	-25.46	6.45	-31.80	7.07
15	2	1	5	0.00	6.45	0.13	5.24	-1.24	6.74	-3.52	5.70
25	1	2		0.00	6.13	2.44	6.96	-4.42	6.95	-9.90	5.66
35	5	3		0.00	6.19	-2.00	6.01	-17.64	6.64	-13.70	6.19
45	3	4		0.00	6.25	-0.15	5.62	-4.56	7.07	-7.37	5.70
55	4	5		0.00	6.19	5.47	5.11	-2.53	6.57	-10.28	6.45

Table B.5: ANOVA table of regression model on S_a of the bulk sections

Source	DF	Adj MS	F-Value	P-Value
Regression	3	0.320	1.280	0.307
X	1	0.886	3.550	0.073
Y	1	0.025	0.100	0.757
Layer no.	1	0.049	0.200	0.663
Error	21	0.250		
Total	24			

Table B.6: ANOVA table on OH S_a after Box-Cox transformation ($\lambda = 0$)

Source	DF	Adj MS	F-Value	P-Value
Layer no.	4	6.36507	306.03	0
OH size	2	0.01887	0.91	0.408
Error	68	0.0208		
Lack-of-Fit	8	0.02188	1.06	0.403
Pure Error	60	0.02065		
Total	74			

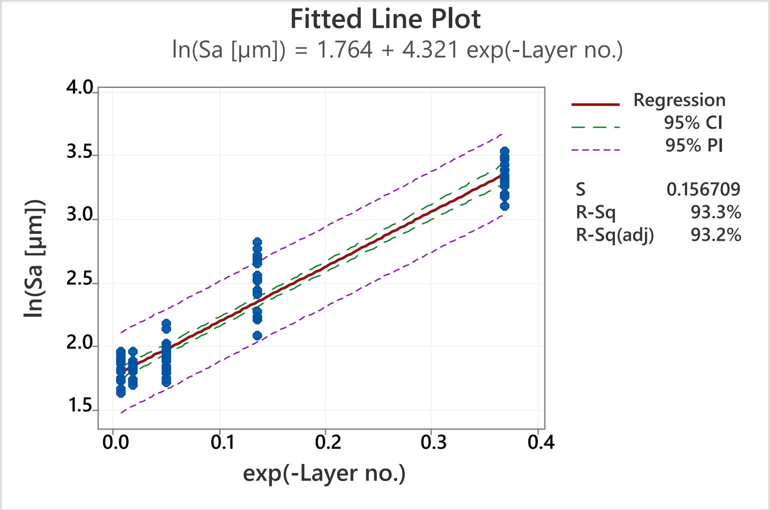

Figure B.25: Linear regression model of S_a vs. *Layer no.* after natural log transformation

Table B.7: Tukey pairwise comparison of *Layer no.* levels. Means that do not share a letter are significantly different.

Layer no.	N	Mean	Grouping
1 (OH)	15	27.6	A
2 (OH)	15	11.7	B
3 (OH)	15	6.7	C
4 (OH)	15	6.1	C
5 (OH)	15	6.1	C
1-5 (Bulk)	15	5.9	C

Table B.8: ANOVA table of linear regression model on raw *Z level* data

Source	**DF**	**Adj MS**	**F-Value**	**P-Value**
Regression	2	8940.1	39.110	0.000
OH size	1	1952.9	8.540	0.005
Layer no.	1	15927.2	69.670	0.000
Error	72	228.6		
Lack-of-Fit	12	114.6	0.460	0.932
Pure Error	60	251.4		
Total	74			

Appendix B.2. Volume analysis data and statistical analyses

The results extracted from the surface maps (Section 3.2) are shown in Table B.9. The details of the statistical analyses are reported in the following subsections.

Appendix B.2.1. Details on the statistical analysis of melted and sintered thickness

The final regression models fitted on t_m and t_s are shown here:

$$t_m = 155.33 - 36.60 * Layer\ no. + 6.23 * OH\ size + 3.80 * (Layer\ no.)^2 \tag{B.3}$$

$$t_s = 22.92 + 5.14 * Layer\ no. + 29.69 * OH\ size \tag{B.4}$$

The results of ANOVA are displayed in Tables B.10 and B.11. The regression function seems to provide a good fitting of the data, with high values of R^2_{adj} (89% and 86%).

Table B.9: Extracted data from XCT reconstruction, *OH size* levels 2 and 3

				OH size					
				2			**3**		
Specimen no.	**X**	**Y**	**Layer no.**	**Melted thickness [µm]**	**Sintered thickness [µm]**	**Pores density [mm-3]**	**Melted thickness [µm]**	**Sintered thickness [µm]**	**Pores density [mm-3]**
11	1	1	1	147.2	80.3	7.6	120.2	98.3	4.3
21	3	2		220.6	103.1	8.8	228.1	139.0	9.5
31	4	3		263.9	93.2	6.1	285.2	132.6	14.0
41	5	4		326.1	96.3	15.9	349.8	131.5	10.1
51	2	5		390.5	110.6	21.0	410.8	140.4	20.9
12	3	1	2	142.3	97.5	7.3	147.7	120.1	6.9
22	5	2		212.0	86.1	8.7	224.0	120.1	8.3
32	2	3		282.9	99.2	21.5	289.2	139.2	22.6
42	4	4		357.6	110.8	49.3	382.4	146.4	32.7
52	1	5		364.6	96.7	32.0	385.3	129.3	31.4
13	5	1	3	145.2	92.2	7.7	145.1	115.0	11.8
23	4	2		229.7	94.1	21.0	244.3	128.9	18.0
33	1	3		308.4	97.3	33.0	303.6	136.2	41.4
43	2	4		370.0	109.3	35.1	376.4	144.7	33.4
53	3	5		417.7	96.8	28.0	436.0	130.6	26.3
14	4	1	4	NA	NA	NA	NA	NA	NA
24	2	2		217.1	77.0	20.0	230.1	111.7	20.7
34	3	3		283.6	99.7	26.4	291.9	129.2	28.3
44	1	4		357.2	109.3	43.6	365.5	135.8	31.5
54	5	5		389.5	95.8	22.3	394.3	139.0	31.9
15	2	1	5	131.4	74.7	3.0	145.2	105.0	6.3
25	1	2		226.4	108.2	11.0	222.5	135.2	8.6
35	5	3		232.0	79.0	17.7	262.7	117.5	16.5
45	3	4		355.3	99.4	12.9	366.9	125.7	22.0
55	4	5		397.3	102.8	15.1	446.5	139.7	16.0

Table B.10: ANOVA table of regression model (B.3) on t_m

Source	DF	Adj MS	F-Value	P-Value
Regression	3	7650.72	158.03	0.000
Layer no.	1	5623.72	116.16	0.000
OH size	1	1101.29	22.75	0.000
Layer no.^{2}	1	2241.25	46.3	0.000
Error	53	48.41		
Lack-of-Fit	10	75.49	1.79	0.091
Pure Error	43	42.11		
Total	56			

Table B.11: ANOVA table of linear regression model (B.4) on t_s

Source	DF	Adj MS	F-Value	P-Value
Regression	2	15534.2	173.33	0.000
Layer no.	1	2786.8	31.09	0.000
OH size	1	25018.6	279.15	0.000
Error	54	89.6		
Lack-of-Fit	11	129	1.62	0.127
Pure Error	43	79.5		
Total	56			

References

[1] Daniel Thomas. Development of Design Rules for SLM. *Thesis*, 2009.

[2] Olaf Diegel, Axel Nordin, and Damien Motte. *A Practical Guide to Design for Additive Manufacturing*. Springer, 1st edition, 2020.

[3] Wadea Ameen, Abdulrahman Al-Ahmari, and Muneer Khan Mohammed. Self-supporting overhang structures produced by additive manufacturing through electron beam melting. *International Journal of Advanced Manufacturing Technology*, 2019.

[4] J Kruth, P Mercelis, J Van Vaerenbergh, and T Craeghs. Feedback control of Selective Laser Melting. pages 1–7, 2007.

[5] M. Matthews, G. Guss, P. DePond, S. Khairallah, G. Tapia, A. Elwany, N. Hodge, A. Anderson, A. Rubenchik, and W. King. Development of intelligent feed-forward methods to reduce part defects in metal powder bed fusion. In *2016 Annual International Solid Freeform Fabrication Symposium*, 2016.

[6] Philip J. DePond, Gabe Guss, Sonny Ly, Nicholas P. Calta, Dave Deane, Saad Khairallah, and Manyalibo J. Matthews. In situ measurements of layer roughness during laser powder bed fusion additive manufacturing using low coherence scanning interferometry. *Materials and Design*, 154:347–359, 2018.

[7] N. E. Hodge, R. M. Ferencz, and J. M. Solberg. Implementation of a thermomechanical model for the simulation of selective laser melting. *Computational Mechanics*, 2014.

[8] Jason C. Fox, Shawn P. Moylan, and Brandon M. Lane. Effect of Process Parameters on the Surface Roughness of Overhanging Structures in Laser Powder Bed Fusion Additive Manufacturing. In *Procedia CIRP*, 2016.

[9] Tao Yang, Tingting Liu, Wenhe Liao, Huiliang Wei, Changdong Zhang, Xiangyuan Chen, and Kai Zhang. Effect of processing parameters on overhanging surface roughness during laser powder bed fusion of AlSi10Mg. *Journal of Manufacturing Processes*, 2021.

[10] F. Calignano, D. Manfredi, E. P. Ambrosio, L. Iuliano, and P. Fino. Influence of process parameters on surface roughness of aluminum parts produced by DMLS. *International Journal of Advanced Manufacturing Technology*, 2013.

[11] Amal Charles, Ahmed Elkaseer, Lore Thijs, and Steffen G. Scholz. Dimensional errors due to overhanging features in laser powder bed fusion parts made of Ti-6Al-4V. *Applied Sciences (Switzerland)*, 2020.

[12] M. Cloots, A. B. Spierings, and K. Wegener. Assessing new support minimizing strategies for the additive manufacturing technology SLM. In *24th International SFF Symposium - An Additive Manufacturing Conference, SFF 2013*, 2013.

[13] Chu Lun Alex Leung, Sebastian Marussi, Robert C. Atwood, Michael Towrie, Philip J. Withers, and Peter D. Lee. In situ X-ray imaging of defect and molten pool dynamics in laser additive manufacturing. *Nature Communications*, 9(1):1–9, 2018.

[14] Cang Zhao, Kamel Fezzaa, Ross W. Cunningham, Haidan Wen, Francesco De Carlo, Lianyi Chen, Anthony D. Rollett, and Tao Sun. Real-time monitoring of laser powder bed fusion process using high-speed X-ray imaging and diffraction. *Scientific Reports*, 7(1):1–11, 2017.

[15] Chris Barrett, Eric MacDonald, Brett Conner, and Fred Persi. Micron-Level Layer-Wise Surface Profilometry to Detect Porosity Defects in Powder Bed Fusion of Inconel 718. *Jom*, 70(9):1844–1852, 2018.

[16] William S. Land, Bin Zhang, John Ziegert, and Angela Davies. In-Situ Metrology System for Laser Powder Bed Fusion Additive Process. *Procedia Manufacturing*, 1:393–403, 2015.

[17] Bin Zhang, John Ziegert, Faramarz Farahi, and Angela Davies. In situ surface topography of laser powder bed fusion using fringe projection. *Additive Manufacturing*, 12:100–107, 2016.

[18] Douglas C. Montgomery. *Design and Analysis of Experiments.* Wiley, 2009.

[19] Richard Leach. *Optical Measurement of Surface Topography*, volume 35. 2011.

[20] P. Bidare, I. Bitharas, R.M. Ward, M.M. Attallah, and A.J. Moore. Fluid and particle dynamics in laser powder bed fusion. *Acta Materialia*, 142:107–120, 2018.

[21] Chunlei Qiu, Chinnapat Panwisawas, Mark Ward, Hector C. Basoalto, Jeffery W. Brooks, and Moataz M. Attallah. On the role of melt flow into the surface structure and porosity development during selective laser melting. *Acta Materialia*, 96:72–79, 2015.

[22] C. Panwisawas, C. L. Qiu, Y. Sovani, J. W. Brooks, M. M. Attallah, and H. C. Basoalto. On the role of thermal fluid dynamics into the evolution of porosity during selective laser melting. *Scripta Materialia*, 105:14–17, 2015.

[23] W. King, A. T. Anderson, R. M. Ferencz, N. E. Hodge, C. Kamath, and S. A. Khairallah. Overview of modelling and simulation of metal powder bed fusion process at Lawrence Livermore National Laboratory. *Materials Science and Technology*, 31(8):957–968, 2015.

[24] Ross Cunningham, Cang Zhao, Niranjan Parab, Christopher Kantzos, Joseph Pauza, Kamel Fezzaa, Tao Sun, and Anthony D. Rollett. Keyhole threshold and morphology in laser melting revealed by ultrahigh-speed x-ray imaging. *Science*, 363(6429), 2019.

[25] A. A. Martin, N. P. Calta, S. A. Khairallah, J. Wang, P. J. Depond, A. Y. Fong, Y.; Thampy, G. M. Guss, A. M. Kiss, K. H. Stone, C. J. Tassone, J. Nelson Weker, M. F. Toney, A. Van Buuren, and M. J. Matthews. Dynamics of pore formation during laser powder bed fusion additive manufacturing. *Nature Communications*, (2019):1–10, 2019.

[26] Nikhil R. Pal and Sankar K. Pal. A review on image segmentation techniques. *Pattern Recognition*, 1993.

[27] Rolf Adams and Leanne Bischof. Seeded Region Growing. *IEEE Transactions on Pattern Analysis and Machine Intelligence*, 1994.

[28] N. Otsu. A Threshold Selection Method from Gray-Level Histograms. *IEEE Transaction on Systems, Man and Cybernetics*, 20(1):62–66, 1979.